8. Gougeon R, Pencharz PB, Sigal RJ. Effect of glycemic control on the kinetics of whole-body protein metabolism in obese subjects with non-insulin-dependent diabetes mellitus during iso-and hypoenergetic feeding. Am J Clin Nutr 1997;65:861–70.
9. Bursztein S, Elwyn DH, Askanazi J, Kinney JM. Energy metabolism, indirect calorimetry, and nutrition. Baltimore, MD: Lippincott Williams & Wilkins, 1989.
10. Compher C, Frankenfield D, Keim N, Roth-Yousey L; Evidence Analysis Working Group. Best practice methods to apply to measurement of resting metabolic rate in adults: a systematic review. J Am Diet Assoc 2006;106:881–903.
11. Frary CD, Johnson RK. Energy. In: Mahan LK, Escott-Stump S. Krause's food & nutrition therapy. 12th ed. St. Louis, MO: Saunders/Elsevier, 2007:22–38.
12. Japan Diabetes Society. Treatment guide for diabetes. Tokyo, Japan: Bunkodo, 2007.
13. Henry CJ. Basal metabolic rate studies in humans: measurement and development of new equations. Public Health Nutr 2005;8:1133–52.
14. Weir JB. New methods for calculating metabolic rate with special reference to protein metabolism. J Physiol 1949;109:1–9.
15. American Diabetes Association. Standards of medical care in diabetes-2011. Diabetes Care 2011;34(suppl 1):S11–61.
16. The Committee of the Japan Diabetes Society on the Diagnostic Criteria of Diabetes Mellitus. Report of the committee on the classification and diagnostic criteria of diabetes mellitus. J Diabetes Invest 2010;1: 212–28.
17. Faber OK, Binder C. C-peptide response to glucagon. A test for the residual beta-cell function in diabetes mellitus. Diabetes 1977;26:605–10.
18. Weyer C, Bogardus C, Pratley RE. Metabolic factors contributing to increased resting metabolic rate and decreased insulin-induced thermogenesis during the development of type 2 diabetes. Diabetes 1999; 48:1607–14.
19. Boden G, Chen X, Stein TP. Gluconeogenesis in moderately and severely hyperglycemic patients with type 2 diabetes mellitus. Am J Physiol Endocrinol Metab 2001;280:E23–30.
20. Nelson DL, Cox MM. Lehninger principles of biochemistry. 5th ed. New York, NY: WH Freeman and Company, 2008.
21. Consoli A, Nurjhan N, Capani F, Gerich J. Predominant role of gluconeogenesis in increased hepatic glucose production in NIDDM. Diabetes 1989;38:550–7.
22. Nuttall FQ, Ngo A, Gannon MC. Regulation of hepatic glucose production and the role of gluconeogenesis in humans: is the rate of gluconeogenesis constant? Diabetes Metab Res Rev 2008;24:438–58.
23. Stump CS, Nair KS. Alterations in protein metabolism in diabetes mellitus. 14th ed. In: Kahn CR, Weir GC, King GL, Jacobson AM, Moses AC, Smith RJ, eds. Joslin's diabetes mellitus. Boston, MA: Joslin diabetes center, 2005:275-90
24. Gougeon R, Morais JA, Chevalier S, Pereira S, Lamarche M, Marliss EB. Determinants of whole-body protein metabolism in subjects with and without type 2 diabetes. Diabetes Care 2008;31:128–33.
25. Dunning BE, Gerich JE. The role of α-cell dysregulation in fasting and postprandial hyperglycemia in type 2 diabetes and therapeutic implications. Endocr Rev 2007;28:253–8.
26. Charlton MR, Nair KS. Role of hyperglucagonemia in catabolism associated with type 1 diabetes. Diabetes 1998;47:1748–56.
27. Nonogaki K. New insights into sympathetic regulation of glucose and fat metabolism. Diabetologia 2000;43:533–49.
28. Anderson EA, Hoffman RP, Balon TW, Sinkey CA, Mark AL. Hyperinsulinemia produces both sympathetic neural activation and vasodilation in normal humans. J Clin Invest 1991;87:2246–52.
29. Fukushima M, Suzuki H, Seino Y. Insulin secretion capacity in the development from normal glucose tolerance to type 2 diabetes. Diabetes Res Clin Pract 2004;66:S37–43.
30. Dela F, von Linstow ME, Mikines KJ, Galbo H. Physical training may enhance β-cell function in type 2 diabetes. Am J Physiol Endocrinol Metab 2004;287:E1024.
31. Funakoshi S, Fujimoto S, Hamasaki A, Fujiwara H, Fujita Y, Ikeda K, Hamamoto Y, Hosokawa M, Seino Y, Inagaki N. Analysis of factors influencing pancreatic beta-cell function in Japanese patients with type 2 diabetes: association with body mass index and duration of diabetic exposure. Diabetes Res Clin Pract 2008;82:353–8.
32. Gougeon R, Lamarche M, Yale JF, Venuta T. The prediction of resting energy expenditure in type 2 diabetes mellitus is improved by factoring for glycemia. Int J Obes Relat Metab Disord 2002;26:1547–52.

Transplant International

Transplant International ISSN 0934-0874

ORIGINAL ARTICLE

Three-dimensional *ex vivo* imaging and analysis of intraportal islet transplants

Hiroyuki Fujimoto,[1] Kentaro Toyoda,[1] Teru Okitsu,[2] Xibao Liu,[1,2] Eri Mukai,[1] Xiaotong Zhuang,[1] Shinji Uemoto,[3] Naoki Mochizuki[4] and Nobuya Inagaki[1,5]

1 Department of Diabetes and Clinical Nutrition, Graduate School of Medicine, Kyoto University, Kyoto, Japan
2 Transplantation Unit, Kyoto University Hospital, Kyoto, Japan
3 Division of Hepato-Pancreato-Biliary Surgery and Transplantation, Department of Surgery, Graduate School of Medicine, Kyoto University, Kyoto, Japan
4 Department of Cell Biology, National Cerebral and Cardiovascular Center Research Institute, Osaka, Japan
5 CREST of Japan Science and Technology Cooperation (JST), Kyoto, Japan

Keywords
allogeneic transplantation, islet transplantation, optical projection tomography, syngeneic transplantation, three-dimensional images.

Correspondence
Nobuya Inagaki, 54 Shogoin Kawahara-cho, Sakyo-ku, Kyoto 606-8507, Japan. Tel.: +81-75-751-3560; fax: +81-75-751-4244; e-mail: inagaki@metab.kuhp.kyoto-u.ac.jp

Conflicts of Interest
All authors have no conflict of interest.

Received: 13 December 2010
Revision requested: 17 January 2011
Accepted: 21 April 2011
Published online: 25 May 2011

doi:10.1111/j.1432-2277.2011.01271.x

Summary

In clinical islet transplantation, because the long-term insulin-independence rate is still poor, a method for detailed analysis of the transplanted islets in the liver after transplantation is required. We have established a novel imaging technique suitable for analysis of transplanted islets in liver using an optical projection tomography (OPT) method. A three-dimensional tomographic image of the transplanted islets in liver was reconstructed. The number of islets transplanted and the number of transplanted islets observed using OPT showed good correlation. The OPT method was used to compare the numbers of transplanted islets in mouse syngeneic and allogeneic transplantation models. Blood glucose concentrations of streptozotocin (STZ)-induced diabetic mice transplanted with syngeneic islets remained normoglycemic and the number of transplanted islets was largely preserved 11 days after transplantation. In mice transplanted with allogeneic islets, hyperglycemia recurred from 7 days after transplantation and the number and the volume of transplanted islets was significantly reduced 11 days after transplantation. These results indicate that OPT imaging and analysis may be a useful tool to quantitatively and sterically evaluation of transplanted islets in liver at the cellular level.

Introduction

Islet transplantation is a promising therapeutic approach for patients with insulin-dependent diabetes mellitus to achieve insulin independence [1,2]. A remarkably high rate of freedom from insulin therapy is achieved in insulin-dependent type 1 diabetic patients after islet transplantation by the Edmonton Protocol [1]. However, it was reported that long-term maintenance of glucose homeostasis without the use of insulin is poor [3]. This decline may be attributed to progressive islet loss as well as to various reactions during and after islet transplantation, including mechanical injury, ischemia, and nonspecific inflammatory reactions [4].

Until now, the total functional volume of islets transplanted intraportally in liver could be monitored only indirectly by measurements such as blood glucose and serum c-peptide levels. Modalities including bioluminescence imaging (BLI) [5–7], magnetic resonance imaging (MRI) [8–11], and positron emission tomography (PET) [12–14] have been used, and transplanted islets were detected by MRI [11] and PET [13] in human. These methods are suitable for *in vivo* examination because they are noninvasive and can be repeated over time. However, islets cannot be evaluated at the cellular level by these methods because the resolution is too low. Conventional immunohistochemical method permit evaluation of beta-cell volume at the subcellular level, but

can only restricted, sliced areas of the sample can be observes. Recently, Hara *et al.* reported subcellular analysis of intact pancreas, but the method can analyze only thin neonatal samples [15]. To investigate engraftment of transplanted islets scattered in solid liver at the subcellular level, another method is required. We have demonstrated an optical projection tomography (OPT) technique for precisely, three-dimensionally evaluating transplanted islets at the cellular level in liver.

Optical projection tomography is a microscopic imaging technique for obtaining three-dimensional, reconstructed images of small biological samples [16]. The principle of OPT is that the light passes through the specimen labeled and cleared for a standard back-projection algorithm to generate a relatively high resolution tomographic image. A three-dimensional image of the specimen is reconstructed using the individual tomographic images. The advantage of OPT is the capability to investigate spatial distribution of such target molecules as RNA and protein without slicing of the target organs and at a higher resolution.

In this report, we show that the number and volume of intraportally transplanted islets in liver can be investigated using OPT analysis. In addition, comparing syngeneic and allogeneic rodent islet transplantation models, we demonstrate that the number and volume of transplanted islets is considerably more decreased in allogeneic islet transplantation than in syngeneic transplantation. Thus, *ex vivo* imaging of intraportal islet transplant using OPT may be a useful tool for evaluation and improvement of islet transplantation outcome.

Materials and methods

Animals

Male C57BL6 Cr Slc mice (Shimizu Laboratory Supplies Co. Ltd, Kyoto, Japan) aged 8–10 weeks were used as recipients and donors and male BALB/c mice (Shimizu Laboratory Supplies Co. Ltd) aged 8 weeks were used as recipients for allogeneic transplantation. All experiments were approved by the Kyoto University Animal Care Committee.

Islet isolation and islet transplantation

Islets were isolated from mouse pancreas using collagenase digestion method [17]; 3–4 ml Hank's Balanced Salt Solution (HBSS) containing 0.5 mg/ml collagenase (Nitta Gelatin, Osaka, Japan) was infused through the common bile duct. The pancreas was dissected and digested at 37 °C for 21 min. Islets were separated from exocrine cells by centrifugation with Ficoll-Conray gradient solution for 10 min. Diabetes was rendered by a single intraperitoneal injection of streptozotocin (STZ) (Nacalai Tesque, Kyoto, Japan), 120 mg/kg body weight, freshly dissolved in 10 mM citrate buffer (pH 4.5). These mice were used as diabetic recipients if the blood glucose concentration was more than 20 mM on two consecutive days. Recipient mice were anesthetized by isoflurane (Forane; Abott, Chicago, IL, USA) during transplantation. Fresh islets in a volume of about 400 μl HBSS were injected into the portal vein and transplanted into the right hepatic lobe as previously reported [18]. For validation of the OPT method, 75, 150 or 300 islets were transplanted into the right hepatic lobe, which was dissected immediately after transplantation. For comparison of syngeneic and allogeneic transplantation, C57BL6 mice ($H\text{-}2^b$) were used as recipients; 300 islets isolated from C57BL6 mice or Balb/c mice ($H\text{-}2^d$) were transplanted, respectively. The blood glucose concentration was determined by glucose meter (Glucocard, Arkley, Japan).

Tissue preparation and immunostaining

Mice with transplanted islets were sacrificed by cervical dislocation. The transplanted right hepatic lobes were dissected clean and immediately immersed for fixation in 4% paraformaldehyde in PBS for 3 h at 4 °C. The fixed samples were washed in PBS and then transferred stepwise to 100% methanol (MeOH) and stored at −20 °C. The immunostaining was performed according to the previous report [19] as follows. The right hepatic lobe was immersed in 15% H_2O_2, 16.7% DMSO solution in MeOH for 24 h to bleach pigmented cells and to reduce auto fluorescence. The liver then was washed in MeOH, which was repeated five times and then kept at −80 °C for at least 1 h before return to room temperature. The organ was rehydrated by Tris Buffered Saline-TritonX (TBST) [0.15 M NaCl (Nacalai Tesque, Kyoto, Japan), 0.1 M Tris (hydroxymethy)aminomethane (Nacalai Tesque, Kyoto, Japan) pH 7.4, and 0.1% Triton X-100 (Nacalai Tesque, Kyoto, Japan)]. TBST containing 10% normal goat serum (Dako Corp., Glostrup, Denmark) and 0.01% sodium azide (Nacalai Tesque, Kyoto, Japan) was used as blocking solution for 24 h. The organ was incubated in insulin antibody (Santa Cruz Biotechnology Inc., Santa Cruz, CA, USA) in 5% DMSO containing blocking solution for 48 h. After washing, Alexa594 goat anti rabbit IgG (Invitrogen, Carlsbad, CA, USA) was used as secondary antibody for 48 h.

Optical projection tomography and image reconstruction

For the observations, the immunostained liver was embedded in 1% agarose gel (low melting point agarose; Sigma Aldrich, St. Louis, MO, USA) to fix the sample.

OPT was performed using an OPT scanner (OPT scanner 3001; Bioptonics, Scotland, UK) according to the manufacturer's instructions [16,19]. The specimens were maintained within the BABB (benzyl alochol/benzyl benzoate 1:2 ratio), rotated to a series of angular positions (0.9° apart) and images were captured at each orientation. High-resolutional tomographic images were reconstructed from raw images by NRecon software (SKYSCAN, Kontich, Belgium). The tomographic images obtained from OPT were reconstructed to three-dimensional form and analyzed by Avizo software (Visualization Science Group, Inc., Burlington, MA, USA). Three-dimensional images of islets and liver were obtained by isosurface treatment. Total volume of all islets was calculated by summation of the selected islets.

Statistical analysis

Data and graph were presented as medians (interquartile range) and statistical analysis was performed with Mann–Whitney's *U*-test. A value of $P < 0.05$ was considered significant.

Results

Observation of transplanted islets in liver by OPT

Transparency of the liver and immunostaining of transplanted islets without sectioning were achieved by the preparation protocols. Figure 1a is a raw OPT image of liver; the insulin-stained transplanted islets are seen as dots in the high magnification image (Fig. 1b, white arrows). One of the tomographic images obtained is shown in Fig. 1c. Vertically reconstructed images are shown in Fig. 1d and e and islets pointed out by arrow and arrowhead in Fig. 1c are located as in Fig. 1d and e, respectively. Some islets appear to be located at the terminal end of the portal vein (Fig. 1c and d) and other islets are located at the wall of the proximal branch of the portal vein (Fig. 1e). Figure 1f is the reconstructed target-specific image of an islet (arrowhead in Fig. 1e) and portal vein. Thus, a three-dimensional image as well as the size and location of transplanted islets in liver can be investigated (Fig. 1g and h and Supplementary movie).

Evaluation of the effectiveness of OPT analysis of transplanted islets in liver

To correlate the number of islets transplanted and the number of islets detected by OPT, we resected and fixed livers immediately after transplantation of a range of numbers of islets. The three-dimensional reconstructed image shows that the number of spots indicating transplanted islets in the right hepatic lobes was increased in accord with the increased dosage (Fig. 2a–c); these numbers are well correlated ($r^2 = 0.9561$) (Fig. 2d). These findings indicate that OPT can be used for quantitative analysis of islets transplanted into liver.

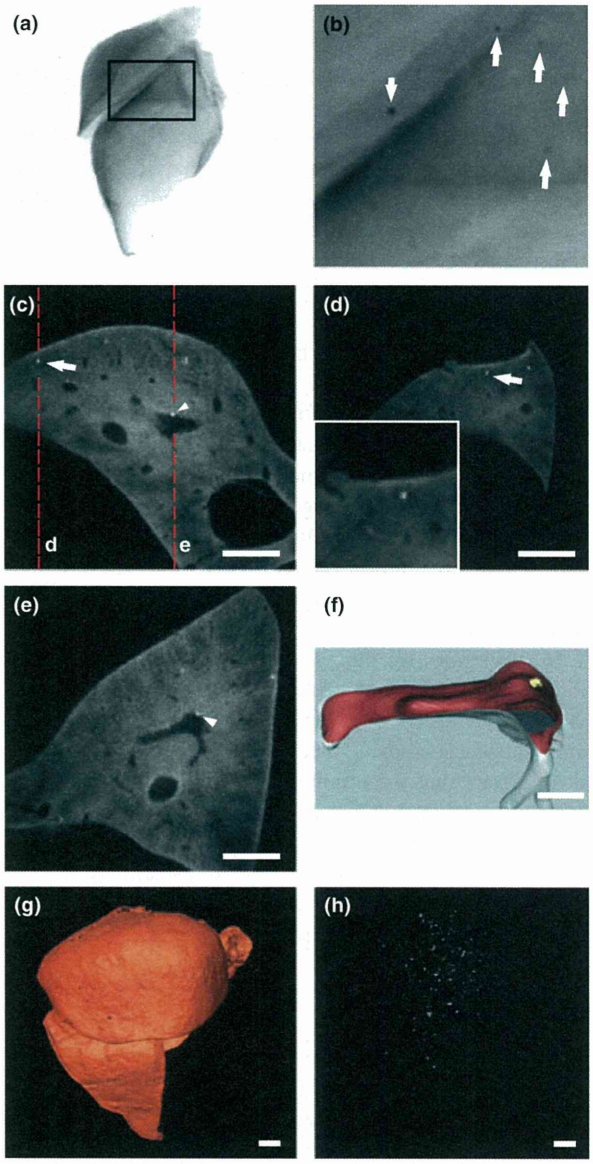

Figure 1 Optical projection tomography (OPT) images of liver containing intraportally transplanted islets. (a) Raw image of islet-transplanted right hepatic lobe, (b) high magnification image [in square of (a)], (c) representative slice image of the transplanted right hepatic lobe; (d and e) vertical slice image of islet with arrow in (c), arrowhead in (c), respectively. (f) Reconstructed three-dimensional image of islet [in (c) and (e), arrowhead] and portal branch. Three-dimensional image of (g) right hepatic lobe; (h) islets (white spots) in liver reconstructed from the same liver sample as (a). Scale bars indicate 1 mm in (c, d, e, g, and h) and 300 μm in (f).

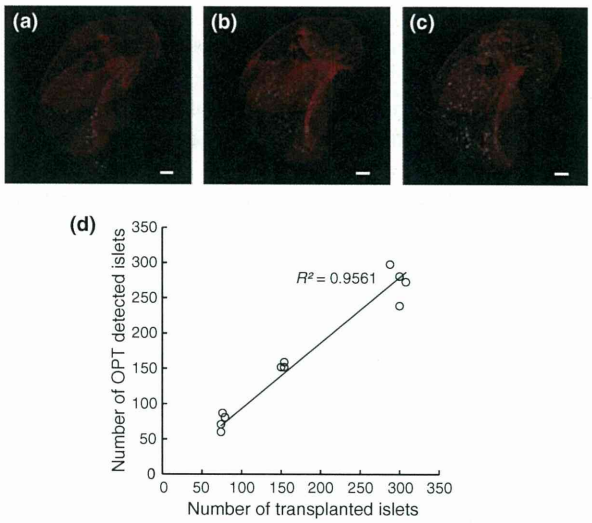

Figure 2 Comparison of the number of islets transplanted with that obtained by optical projection tomography (OPT) analysis. Representative OPT image of recipient liver transplanted with (a) 75, (b) 150, and (c) 300 islets, respectively. (d) Correlation of the number of islets transplanted and OPT-detected islets. Scale bar indicates 1 mm.

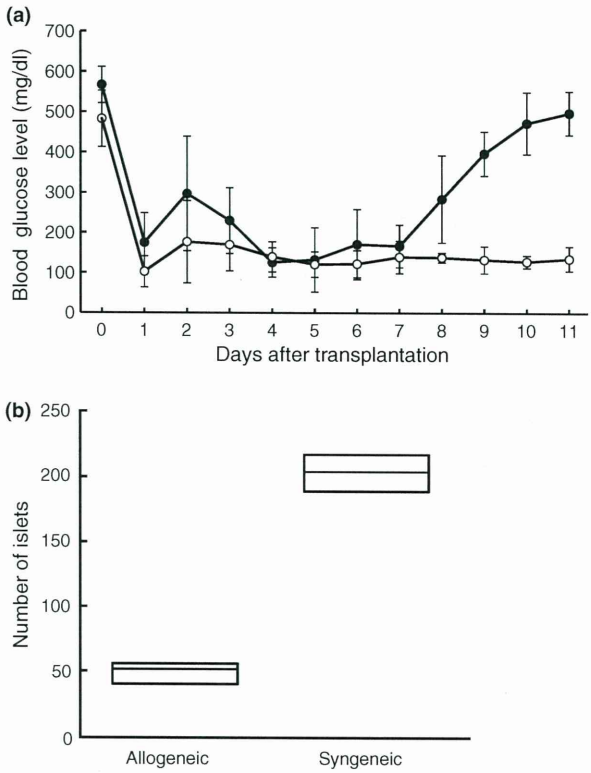

Figure 3 Glycemic level and number of islets of streptozotocin (STZ)-induced diabetic mice after syngeneic and allogeneic islet transplantation. (a) Random blood glucose level of recipients (open circles: syngeneic transplantation, filled circles: allogeneic transplantation). (b) Number of transplanted islets in syngeneic and allogeneic transplantation 11 days after transplantation.

Optical projection tomography analysis of islet grafts under syngeneic and allogeneic conditions

To evaluate the time course of transplanted islets in syngeneic and allogeneic conditions, we analyzed the number and volume of islets intraportally transplanted in liver of STZ-induced diabetic mice. Blood glucose concentrations under both syngeneic and allogeneic conditions were normoglycemic until a week after transplantation. However, blood glucose concentrations under allogeneic conditions thereafter became hyperglycemic, while those under syngeneic conditions remained normoglycemic (Fig. 3a). The islet-containing livers were resected on day 11 for analysis using OPT method. The number of islets in the syngeneic condition was dramatically greater than that in the allogeneic condition [52 (IQR 16.5) vs. 203 (28.5), respectively, $P < 0.05$] (Fig. 3b).

In OPT-detected islets classified by size, the number in each category was significantly greater in syngeneic than in allogeneic conditions and showed a similar histogram pattern (Fig. 4a). Total volume of islets in syngeneic condition was dramatically greater than that in allogeneic condition [8.6 (2.7) vs. 35.3 (10.1) ($\mu m^3 \times 10^6$)], respectively, ($P < 0.05$) (Fig. 4b).

Discussion

In this study, we demonstrate that islets transplanted intraportally in liver can be analyzed at the cellular level using OPT method, which permits three-dimensional analysis of the distribution of the islets in the liver. Comparing syngeneic and allogeneic islet transplantation models, we show by OPT that the volume of transplanted islets differs significantly at the cellular level.

One of main problems in clinical islet transplantation, poor long-term achievement of insulin independence, is primarily attributed to graft loss caused by various stressors upon transplantation [4]. When islets are injected intraportally, each of them is thought to locate at the respective branched end of the portal vein in liver. In modalities such as BLI, MRI, and PET, only PET allows quantification of graft volume, but the resolution is still too low for detailed analysis of the transplanted islets. On the other hand, while the resolution of conventional immunohistochemistry is high, only restricted slices of the engrafted organ can be analyzed using this method.

Optical projection tomography, a newly developed method, is reported to permit analysis of a sample at resolution as high as 5 μm. Recently, Alanentalo *et al.* performed detailed analysis of NOD mice during progression

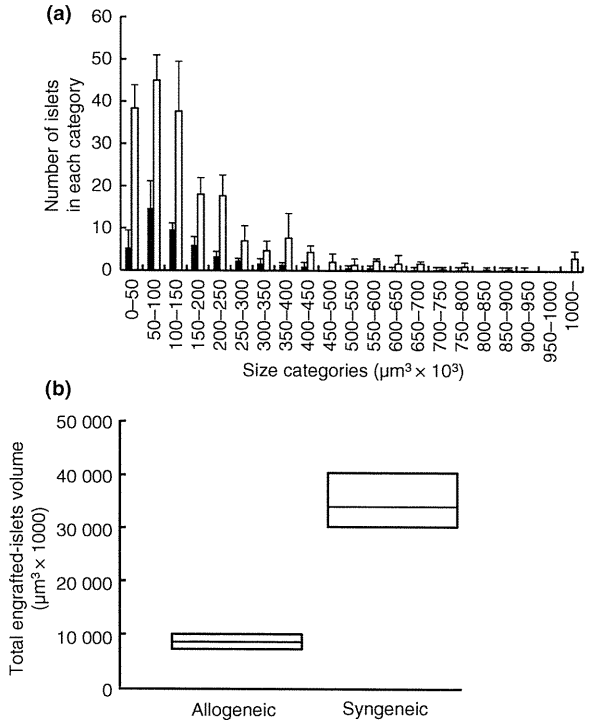

Figure 4 Quantitative analysis of transplanted islets in syngeneic and allogeneic model. (a) Size distribution of transplanted islets. (b) Total volume of transplanted islets in liver obtained using optical projection tomography (OPT) analysis.

of type 1 diabetes and showed that a reduction in volume of native islets in pancreas could be detected and quantified using the OPT method [20]. We have used OPT method for the first time in the intraportal islet transplantation model and confirm the efficacy of this method of islet imaging (Figs 1 and 2).

However, there are several limitations in use of the OPT method. It can be performed only *ex vivo*, and noninvasive, repeated observation is not possible. In this context, PET and MRI are suitable for *in vivo*, repeated monitoring of transplanted islets. In addition, the maximum sample size for analysis using OPT is about 2 cm. The OPT method also is not clinically applicable as it would require a large liver biopsy.

The OPT method is useful for evaluating small organs of small animals such as rodents, as in our present study. Indeed, using rodent islet transplantation models, the OPT method clearly shows quantitative difference of grafts in liver in syngeneic and allogeneic conditions. In this investigation, the OPT method revealed that 83% of the transplanted islets were lost in the allogeneic condition while about 70% were preserved in the syngeneic condition. Moreover, calculated beta-cell volume in the allogeneic condition was significantly reduced to 24.2% of that in the syngeneic condition (Figs 3b and 4b). This remarkable graft loss by allogeneic immune reaction seems not to be related to the size of the islet graft, as there was no difference in size distribution histogram between the two conditions (Fig. 4a). The OPT method also clearly shows the sites where islets adhere and are engrafted in the portal vein. Further investigation is required to determine the effect of islet location on islet engraftment.

In conclusion, we have constructed three-dimensional images of transplanted islets in liver using an OPT method that permits detailed analysis of transplanted islets in liver. This method should be useful for islet transplantation study.

Authorship

HF: designed the study, performed the study, collected the data, analyzed the data, and wrote the paper. KT: designed the study, performed the study, and wrote the paper. TO, SU, and NM: designed the study. XL, EM, and XZ: performed the study. NI: designed the study, wrote the paper.

Funding

This work was supported by a Research Grant from the Ministry of Health, Labour, and Welfare of Japan, and from the Ministry of Education, Culture, Sports, Science, and Technology of Japan, and the Program for Promotion of Fundamental Studies in Health Sciences of the National Institute of Biomedical Innovation (NIBIO), and also by Kyoto University Global COE Program "Center for Frontier Medicine".

Supporting information

Additional Supporting Information may be found in the online version of this article:

Clip S1. Three dimensional image of islets transplanted in liver – Transplanted islets were scattered in liver. This image was reconstructed by software "Avizo".

Please note: Wiley-Blackwell are not responsible for the content or functionality of any supporting materials supplied by the authors. Any queries (other than missing material) should be directed to the corresponding author for the article.

References

1. Shapiro AM, Lakey JR, Ryan EA, *et al.* Islet transplantation in seven patients with type 1 diabetes mellitus using a

glucocorticoid-free immunosuppressive regimen. *N Engl J Med* 2000; **343**: 230.
2. Shapiro AM, Ricordi C, Hering B. Edmonton's islet success has indeed been replicated elsewhere. *Lancet* 2003; **362**: 1242.
3. Ryan EA, Paty BW, Senior PA, *et al.* Five-year follow-up after clinical islet transplantation. *Diabetes* 2005; **54**: 2060.
4. Ricordi C, Strom T. Clinical islet transplantation: advances and immunological challenges. *Nat Rev Immunol* 2004; **4**: 259.
5. Lu Y, Dang H, Middleton B, *et al.* Bioluminescent monitoring of islet graft survival after transplantation. *Mol Ther* 2004; **9**: 428.
6. Fowler M, Virostko J, Chen Z, *et al.* Assessment of pancreatic islet volume after islet transplantation using *in vivo* bioluminescence imaging. *Transplantation* 2005; **79**: 768.
7. Chen X, Zhang X, Larson CS, Baker MS, Kaufman DB. *In vivo* bioluminescence imaging of transplanted islets and early detection of graft rejection. *Transplantation* 2006; **81**: 1421.
8. Evgenov NV, Medarova Z, Guangping D, Bonner-Weir S, Moore A. *In vivo* imaging of islet transplantation. *Nat Med* 2006; **12**: 144.
9. Evgenov NV, Medarova Z, Pratt J, *et al. In vivo* imaging of immune rejection in transplanted pancreatic islets. *Diabetes* 2006; **55**: 2419.
10. Tai JH, Foster P, Rosales A, *et al.* Imaging islets labeled with magnetic nanoparticles at 1.5 Tesla. *Diabetes* 2006; **55**: 2931.
11. Saudek F, Jirák D, Girman P, *et al.* Magnetic resonance imaging of pancreatic islets transplanted into the liver in humans. *Transplantation* 2010; **90**: 1602.
12. Lu Y, Dang H, Middleton B, *et al.* Noninvasive imaging of islet grafts using positron-emission tomography. *Proc Natl Acad Sci USA* 2006; **103**: 11294.
13. Toso C, Zaidi H, Morel P, *et al.* Positron-emission tomography imaging of early events after transplantation of islets of Langerhans. *Transplantation* 2005; **79**: 353.
14. Kim SJ, Doudet DJ, Studenov AR, *et al.* Quantitative micro positron emission tomography (PET) imaging for the *in vivo* determination of pancreatic islet graft survival. *Nat Med* 2006; **12**: 1423.
15. Miller K, Kim A, Kilimnik G, *et al.* Islet formation during the neonatal development in mice. *PLoS ONE* 2009; **4**: e7739.
16. Sharpe J, Ahlgren U, Perry P, *et al.* Optical projection tomography as a tool for 3D microscopy and gene expression studies. *Science* 2002; **296**: 541.
17. Sutton R, Peters M, Mcshane P, Gray DWR, Morris PJ. Isolation of rat pancreatic-islets by ductal injection of collagenase. *Transplantation* 1986; **42**: 689.
18. Yonekawa Y, Okitsu T, Wako K, *et al.* A new mouse model for intraportal islet transplantation with limited hepatic lobe as a graft site. *Transplantation* 2006; **82**: 712.
19. Alanentalo T, Asayesh A, Morrison H, *et al.* Tomographic molecular imaging and 3D quantification within adult mouse organs. *Nat Methods* 2007; **4**: 31.
20. Alanentalo T, Hornblad A, Mayans S, *et al.* Quantification and three-dimensional imaging of the insulitis-induced destruction of β-cells in murine type 1 diabetes. *Diabetes* 2010; **59**: 1756.

Systems analysis of GLP-1 receptor signaling in pancreatic β-cells

Yukari Takeda, Akira Amano, Akinori Noma, Yasuhiko Nakamura, Shimpei Fujimoto and Nobuya Inagaki

Am J Physiol Cell Physiol 301:C792-C803, 2011. First published 6 July 2011;
doi:10.1152/ajpcell.00057.2011

Am J Physiol Cell Physiol 301: C792–C803, 2011.
First published July 6, 2011; doi:10.1152/ajpcell.00057.2011.

Systems analysis of GLP-1 receptor signaling in pancreatic β-cells

Yukari Takeda,[1] Akira Amano,[2] Akinori Noma,[2] Yasuhiko Nakamura,[1] Shimpei Fujimoto,[1] and Nobuya Inagaki[1]

[1]*Department of Diabetes and Clinical Nutrition, Graduate School of Medicine, Kyoto University, Kyoto; and* [2]*Faculty of Bioinformatics, Ritsumeikan University, Kusatsu City, Japan*

Submitted 3 March 2011; accepted in final form 28 June 2011

Takeda Y, Amano A, Noma A, Nakamura Y, Fujimoto S, Inagaki N. Systems analysis of GLP-1 receptor signaling in pancreatic β-cells. *Am J Physiol Cell Physiol* 301: C792–C803, 2011. First published July 6, 2011; doi:10.1152/ajpcell.00057.2011.—Glucagon-like peptide-1 (GLP-1) elevates intracellular concentration of cAMP ([cAMP]) and facilitates glucose-dependent insulin secretion in pancreatic β-cells. There has been much evidence to suggest that multiple key players such as the GLP-1 receptor, G_s protein, adenylate cyclase (AC), phosphodiesterase (PDE), and intracellular Ca^{2+} concentration ($[Ca^{2+}]$) are involved in the regulation of [cAMP]. However, because of complex interactions among these signaling factors, the kinetics of the reaction cascade as well as the activities of ACs and PDEs have not been determined in pancreatic β-cells. We have constructed a minimal mathematical model of GLP-1 receptor signal transduction based on experimental findings obtained mostly in β-cells and insulinoma cell lines. By fitting this theoretical reaction scheme to key experimental records of the GLP-1 response, the parameters determining individual reaction steps were estimated. The model reconstructed satisfactorily the dynamic changes in [cAMP] and predicted the activities of cAMP effectors, protein kinase A (PKA), and cAMP-regulated guanine nucleotide exchange factor [cAMP-GEF or exchange protein directly activated by cAMP (Epac)] during GLP-1 stimulation. The simulations also predicted the presence of two sequential desensitization steps of the GLP1 receptor that occur with fast and very slow reaction rates. The cross talk between glucose- and GLP-1-dependent signal cascades for cAMP synthesis was well reconstructed by integrating the direct regulation of AC and PDE by $[Ca^{2+}]$. To examine robustness of the signaling system in controlling [cAMP], magnitudes of AC and PDE activities were compared in the presence or absence of GLP-1 and/or the PDE inhibitor IBMX.[1]

adenylyl cyclase; glucagon-like peptide-1; model stimulation; phosphodiesterase

UPON ELEVATION of plasma glucose concentration ([glucose]), pancreatic β-cells generate bursts of action potentials to induce cyclic changes in $[Ca^{2+}]$ (55) and regulate pulsatile insulin release (25). This glucose-dependent insulin secretion is synergistically enhanced by incretin hormones, which are released upon meal ingestion from endocrine cells distributed over the intestinal tract (16). The incretin hormones include glucose-dependent insulinotropic peptide (GIP) and glucagon-like peptide-1 (GLP-1). GLP-1 is more effective than GIP to improve deteriorated incretin effect in diabetes and is widely used to treat patients with Type 2 diabetes (45). Elucidation of GLP-1 signaling system in β-cells, therefore, has been an extensive target of experimental studies. To date, it has been well established that GLP-1 activates adenylate cyclases (ACs) through binding to its G protein-coupled receptor and increases [cAMP], the key signal underlying the insulinotropic effects (17, 62).

The [cAMP] is determined primarily by the balance between cAMP production by ACs and degradation by phospodiesterases (PDEs) (8). The activities of several isoforms of AC and PDE expressed in β-cells are controlled by $[Ca^{2+}]$ (11, 28), which is regulated by Ca^{2+}-permeable ion channels and transporters as well as Ca^{2+} release and uptake by the endoplasmic reticulum (ER). The increase in [cAMP] subsequently activates protein kinase A (PKA) and exchange protein directly activated by cAMP (Epac), modulating the activities of multiple ion channels at the plasma membrane (26, 31, 35, 41, 42, 57) and ER (27, 36, 64), which in turn modify the pattern of Ca^{2+} transients. PKA and Epac also have direct effects on proteins that are involved in exocytosis of insulin vesicles (30), and thus the fine regulation of [cAMP] is critical for the adequate insulinotropic effects of GLP-1. However, since multiple signaling factors are involved in regulating [cAMP], the kinetic aspects of the reaction cascade during GLP-1 stimulation have not yet been determined in pancreatic β-cells.

To overcome this difficulty, we developed a mathematical model of GLP-1 receptor signal transduction. We adopted a strategy of estimating individual reaction rates and model parameters by fitting the theoretical reaction scheme to a variety of key experimental findings published to date (3, 11, 54, 66) in both β-cells and insulinoma cell lines. The model thus developed was validated by reconstructing the dynamic changes in [cAMP] during GLP-1 stimulation in the presence and absence of 3-isobutyl-1-methylxanthine (IBMX) observed under various experimental conditions. The model well-simulated GLP-1-induced [cAMP] elevation and predicted the activities of cAMP effectors PKA and Epac as a function of GLP-1. The simulation analysis revealed the presence of two transition steps of receptor desensitization that occur with fast and slow kinetics. The molecular basis for synergistic relationship between glucose and GLP-1 signaling in the cAMP synthesis were clarified by calculating the direct regulation of AC and PDE by $[Ca^{2+}]$. Finally, the robustness of the signaling system in controlling [cAMP] was examined by comparing the AC and PDE activities in the presence or absence of GLP-1 and/or the PDE inhibitor.

Glossary

[L]	GLP-1 (ligand)
[R]	free GLP-1receptor
$[R_t]$	total GLP-1 receptor
$[R_a]$	active GLP-1 receptor
$[R_{D1}]$	desensitized GLP-1 receptor in state 1
$[R_{D2}]$	desensitized GLP-1 receptor in state 2
[LR]	GLP-1 receptor bound with ligand

[1] This article is the topic of an Editorial Focus by Harvey (29a).

Address for reprint requests and other correspondence: N. Inagaki, 54 Shogoin, Kawahara-cho, Sakyo-ku, Kyoto-shi, Kyoto, Japan.

[LRG]	GLP-1 receptor bound with ligand and G_s
[G_t]	total G_s protein
[G]	G_s complex
[$G_{\beta\gamma}$]	β and γ subunit of G_s
[G_αGTP]	total GTP-bound α subunit of G_s
[G_αGDP]	GDP-bound α subunit of G_s
V_{AC_t}	total adenylate cyclase activity
V_C	activity of adenylate cyclase with G protein unbound
$V_{max\_AC\_t}$	Maximum activity of V_{AC}
V_{AC_G}	activity of adenylate cyclase with GαGTP
$V_{max\_AC\_G}$	maximum activity of V_{AC_G}
f_{Cd_AC}	fraction of Ca_xCaM-dependent V_{AC_G}
V_{Cd_AC}	Ca_xCaM-dependent component of V_{AC_G}
[CaM]	Calmodulin
[Ca_xCaM]	Calmodulin bound with Ca^{2+} ions ([Ca_3CaM]+[Ca_4CaM])
[Ca_3CaM]	Calmodulin bound with 3 Ca^{2+} ions
[Ca_4CaM]	Calmodulin bound with 4 Ca^{2+} ions
V_{PDE}	activity of phosphodiesterase
V_{max_PDE}	maximum activity of V_{PDE}
K_{mL}	low K_m of PDE
K_{mH}	high K_m of PDE
f	fraction of PDE with K_{mL}
f_{Cd_PDE}	fraction of Ca_xCaM-dependent V_{PDE}
V_{Cd_PDE}	Ca_xCaM-dependent component of V_{PDE}

METHODS

A minimal model of the GLP-1 receptor signaling transduction in pancreatic β-cells was constructed. Parameters to define the model, including concentrations, binding constants (K_d) of signaling factors, maximum activity (V_{max}) and half-maximal effective concentration ($K_{1/2}$) of substances for activation of enzymes, rate constants, and various magnitude factors of kinetic equations are listed in APPENDIX I. The time-based integration of six differential equations (*Eqs. 3–8*) were performed using the Euler method with a time step of <2 ms on the Microsoft Visual Studio platform. The units of time and substrate concentrations are secons and millimolar (indicated otherwise), respectively.

Activation of GLP-1 receptor. Figure 1 shows the reaction scheme of the minimal model of the GLP-1 receptor cascade. Active receptors may form three different conformations: free receptor (R), ligand (L)-bound receptor (LR), and the Gs-bound LR complex (LRG). Binding reactions indicated by black arrows were assumed to be much faster than the rest of reactions associated with conformational changes (22), and thus an instantaneous equilibrium was assumed for the reactions enclosed within the red rectangle. The dissociation constant (K_d) for GLP-1 binding to the receptor has been determined in expression systems (43, 65), whereas K_d for LR and G was estimated by fitting the [GLP-1]-dependent [cAMP] accumulation (66). In calculating the reaction cascade, total amounts [R_t] and [G_t] were conserved by applying *Eqs. 1* and *2*, respectively.

$$[R_t] = [R_a] + [R_{D1}] + [R_{D2}] \quad \text{Where } [R_a] = [R] + [LR] + [LRG]. \tag{1}$$

$$[G_t] = [G_{\alpha\beta\gamma}] + [G_{\beta\gamma}] \quad \text{Where } [G_{\alpha\beta\gamma}] = [G] + [LRG] \tag{2}$$

Upon ligand binding, the GLP-1 receptor undergoes desensitization through phosphorylation by unknown mechanisms (67). Although the molecular mechanism has not been elucidated, the computer simulation of the spontaneous decay in [cAMP] during continuous stimulation with GLP-1 (see Fig. 3) as well as desensitized [cAMP] production after preconditioning of GLP-1 receptors (see Fig. 4) suggested the presence of two sequential desensitization states R_{D1} and R_{D2}. We assume that the first desensitization step to R_{D1} occurs from the ligand-bound form of the receptor, (LR + LRG), followed by the second transition to R_{D2} with a recovery steps to R_a (see Fig. 1). The rate constants for the time-dependent desensitization were determined by fitting the kinetic sheme to experimental recordings, and the time-dependent changes in [R_{D1}] and [R_{D2}] are defined with *Eqs. 3* and *4*, respectively.

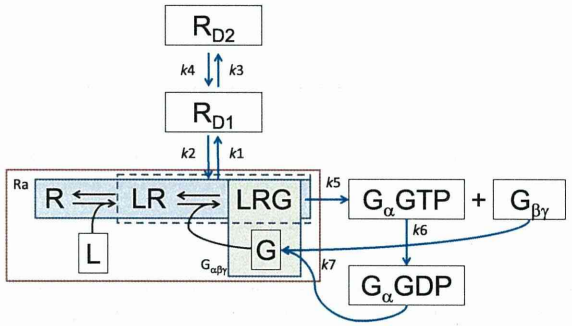

Fig. 1. Reaction scheme of glucagon-like peptide-1 (GLP-1) receptor activation. The receptor takes five different conformations: R, free receptor; LR, ligand (L)-bound form; LRG, G_s-bound LR complex; R_{D1}, desensitized receptor at the state D1 with faster kinetics defined by rate constants *k*1 and *k*2; and R_{D2}, desensitized receptor at the state D2 with the very slow kinetics defined by rate constants *k*3 and *k*4. The desensitization to R_{D1} occurs only from the ligand bound form (LR and LRG) with *k*1, and the recovery to active receptos (R_a) (= R + LR + LRG) with *k*2. States of G_s protein include $G_{\alpha\beta\gamma}$, heterotrimeric complex (for [G] and [LRG]) and dissociated subunits G_αGTP, G_αGDP, and $G_{\beta\gamma}$. Time-dependent changes in conformations of G protein are calculated by rate constants of G_s dissociation into G_αGTP and $G_{\beta\gamma}$ subunits (*k*5), subsequent hydrolysis of GTP (*k*6), and reassociation of G_αGDP with $G_{\beta\gamma}$ (*k*7). The reaction steps marked with a black arrow were calculated assuming instantaneous equilibrium, whereas those marked with blue arrows were calculated by the time-based integration using the Euler method. When calculating the instantaneous equilibrium enclosed with the red rectangle, the constraint of mass conservation was applied to the sum of (R + LR + LRG) and (G + LRG), respectively, at each time step.

$$d[R_{D1}]/dt = k1 \cdot ([LR] + [LRG]) - k2 \cdot [R_{D1}] - k3 \cdot [R_{D1}] + k4 \cdot [R_{D2}] \tag{3}$$

$$d[R_{D2}]/dt = k3 \cdot [R_{D1}] - k4 \cdot [R_{D2}] \tag{4}$$

The kinetics for the activation and deactivation of G protein are calculated by rate constants of G dissociation into G_αGTP and $G_{\beta\gamma}$ subunits and subsequent hydrolysis of GTP (APPENDIX I), which have been biochemically investigated (5, 56). The time-dependent changes in [G_αGTP], [G_αGDP], and [$G_{\beta\gamma}$] are described by the following differential equations:

$$d[G_\alpha GTP]/dt = k5 \cdot [LRG] - k6 \cdot [G_\alpha GTP] \tag{5}$$

$$d[G_\alpha GDP]/dt = k6 \cdot [G_\alpha GTP] - k7 \cdot [G_\alpha GDP] \cdot [G_{\beta\gamma}] \tag{6}$$

$$d[G_{\beta\gamma}]/dt = k5 \cdot [LRG] - k7 \cdot [G_\alpha GDP] \cdot [G_{\beta\gamma}] \tag{7}$$

AC and PDE activities. The level of [cAMP] is determined by the balance between production rate (V_{AC_t}) and degradation rate (V_{PDE}) by ACs and PDEs, respectively (*Eq. 8*).

$$\frac{d[cAMP]}{dt} = V_{AC\_t} - V_{PDE} \tag{8}$$

At least nine different isoforms of membrane-bound AC have been identified (29). In pancreatic β-cells, ACVIII was suggested to play a predominant role in synthesis of cAMP during GLP-1 stimulation of β-cells (53). The modulation of ACVIII by both Ca^{2+}-bound calmodulin (Ca_xCaM) and $G_{s\alpha}$GTP would provide the molecular basis for synergistic relationship between glucose and GLP-1 stimulation in the cAMP synthesis (11). In addition to this adaptable component

(V_{AC_G}), a basal component (V_{AC}) was assumed to maintain the resting [cAMP] in the absence of agonists. Thus the total activity of ACs (V_{AC_t}) is given by a sum of V_{AC} and V_{AC_G} (*Eqs. 9–11*).

$$V_{AC\_t} = V_{AC} + V_{AC\_G} \quad (9)$$

$$V_{AC} = V_{max\_AC} \cdot \frac{0.0004}{0.0004 + G_\alpha GTP} \cdot \frac{[ATP]}{[ATP] + 1.03} \quad (10)$$

$$V_{AC\_G} = V_{max\_AC\_G} \cdot \frac{G_\alpha GTP}{0.0004 + G_\alpha GTP} \cdot \frac{[ATP]}{[ATP] + 0.315} \times \left((1 - f_{Cd\_AC}) + f_{Cd\_AC} \cdot \frac{[Ca_3CaM] + [Ca_4CaM]}{[Ca_3CaM] + [Ca_4CaM] + 0.000348} \times \frac{0.075}{0.075 + [Ca^{2+}]} \right) \quad (11)$$

The $G_\alpha GTP$-dependent activation of AC was calculated with a $K_{1/2}$ determined by Sunahara and colleagues (58). An [ATP] of 3 mM was used in the present study, and the $K_{1/2}$ of [ATP] defining the substrate dependency of V_{AC} and V_{AC_G} were adopted from Dessauer et al. (13). The term for Ca^{2+}-dependent regulation of V_{AC_G} in *Eq. 11* was originally developed in *Aplysia* neurons (69) and was modified to fit the ACVIII activity (21) in the β-cell model by Fridlyand et al. (23). *Eq. 11* contains both Ca_xCaM ([Ca_3CaM]+[Ca_4CaM])-mediated activation and Ca^{2+}-dependent inhibition. We additionally introduced f_{Cd_AC}, the fraction of Ca_xCaM-dependent V_{AC_G}. A [Ca^{2+}] of 500 nM was assumed under a high-glucose condition and a resting [Ca^{2+}] of 100 nM for a lower glucose concentration used in experiments (18, 33, 60). An instantaneous equilibrium was assumed for the binding of Ca^{2+} to CaM using the association and dissociation rate constants given by Yu and colleagues (69). The V_{AC_t} was determined at 1.8 μM/s from the initial rate of rise (dashed line in Fig. 3*A*) of [cAMP] evoked by GLP-1 in the presence of high [IBMX] > 250 μM and [glucose] > 20 mM. Based on this estimation, V_{max} of AC activities (V_{max_AC} and $V_{max\_AC\_G}$) and fractions (f) of the Ca^{2+}-dependent component of V_{AC_G}(f_{Cd_AC}) were optimized (see APPENDIX I) by reconstructing experimental findings with the whole reaction scheme.

In β-cells, it has been suggested that several PDE isoforms (1C, 3B, 4, 8B, and 10A) are involved in regulation of insulin secretion (15, 51). However, the fractional contribution of each isoform to cAMP degradation in intact cells has not yet been determined. Sams and Montague (54) observed over 70% of total PDE activity in the supernatant fraction of an homogenate of islets of Langerhans. Their kinetic analysis of the soluble PDEs suggested the presence of at least two fractions with different activities, as indicated by two linear components (dashed and solid black lines) in the Lineweaver-Burk plot (Fig. 2). We reevaluated the experimental results by fitting the data with a sum of two Michaelis-Menten functions (*Eq. 12*) in the present study.

$$V_{PDE} = V_{max\_PDE} \cdot \left(\frac{f \cdot [cAMP]}{[cAMP] + K_{mL}} + \frac{(1 - f) \cdot [cAMP]}{[cAMP_f] + K_{mH}} \right) \quad (12)$$

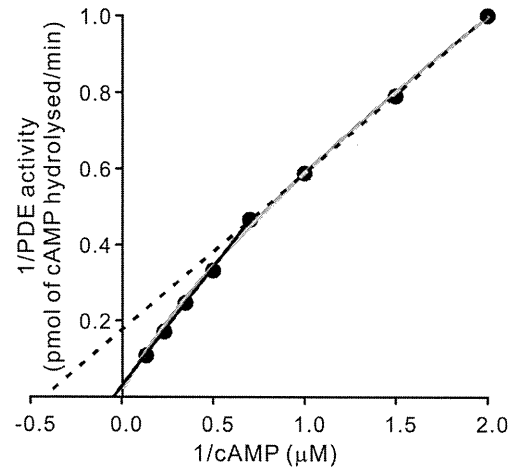

Fig. 2. Determination of K_m values of phosphodiesterase (PDE) based on experimental Lineweaver-Burk plots. Filled circles and fitted (dotted and black) lines are reproduction of experimental data (54) determined in guinea pig islets. The properties of the PDE activity components were reevaluated by fitting the experimental results with *Eq. 12* (solid gray line).

The fitting (gray curve in Fig. 2) determined the K_m values (K_{mL} and K_{mH}) and f of the two components. V_{PDE} thus reflects the sum of all PDE activities.

Since Ca_xCaM-sensitive PDE1C plays a functional role in degradation of cAMP in the β-cell lines βTC3 (28) and MIN6 (38), a Ca^{2+}-dependent component was added to the PDE model (*Eq. 13*).

$$V_{PDE} = V_{max\_PDE} \cdot \left(\frac{f \cdot [cAMP]}{[cAMP] + K_{mL}} + \frac{(1 - f) \cdot [cAMP]}{[cAMP] + K_{mH}} \right) \left[(1 - f_{Cd\_PDE}) + f_{Cd\_PDE} \cdot \frac{[Ca_3CaM] + [Ca_4CaM]}{[Ca_3CaM] + [Ca_4CaM] + 0.000348} \right] \quad (13)$$

The half-maximal value of Ca_xCaM for the stimulation of PDE (68) was adopted from the PDE model developed for β-cells (23), and f_{Cd_PDE} reflects the fraction of the Ca_xCaM-dependent component of the enzyme. Given the [cAMP]s determined under various experimental conditions (Table 1), V_{max_PDE} and f_{Cd_PDE} (APPENDIX I) were finely adjusted by reconstructing these experimental findings using 100 or 500 nM [Ca^{2+}] according to the [glucose] used in experiments.

In experimental studies, the rise in [cAMP] evoked by GLP-1 saturates even in the presence of a maximal inhibitory concentration of IBMX, indicating that some fraction of PDE activity still remained, controlling [cAMP]. Ahmad and colleagues (1) showed that ~80% of the soluble PDE activity in a β-cell line (BRIN-BD11 cells) was blocked by [IBMX] > 200 μM, and thus we assumed that the

Table 1. *Comparison of [cAMP] between experimental measurements in rat primary pancreatic β-cells and model simulations under control conditions and after 15 min stimulation with GLP-1 with or without IBMX*

	Experimental Data	Simulation Result	Experimental Data	Simulation Result
Experimental conditions:	1.4 mM Glucose	100 nM Ca^{2+}	20 mM Glucose	500 nM Ca^{2+}
cAMP levels, μM				
Resting (control)	3.4	1.6	3.2	1.4
10 nM GLP-1		4.2		5.6
Resting w/ IBMX	10.5	12.0	11.7	10.3
10 nM GLP-1w/ IBMX	38.2	37.0	55.2	57.6

The cAMP levels were indicated in units of fmol·10^3 $cells^{-1}$ in the experimental work (11), and we converted these units to μM by assuming the cytoplasmic volume of a single β-cell [764 fL; (10)]. Administration of IBMX (250 μM) was simulated by decreasing PDE activity by 80%. See text for definitions of abbreviations.

IBMX-insensitive PDE8 may contribute 20% PDE activity in the presence of a high [IBMX].

PKA and Epac activities. Although pancreatic β-cells most likely express both PKA type I and II (2, 37, 39), the isoform predominantly regulating the insulinotropic effect of GLP-1 has not been investigated. Since K_d of PKA type I [2.9 μM (9)] and the half-maximal [cAMP] for the activation of type II [$K_{1/2}$ = 2~3 μM (7)] were very similar, we included one hypothetical type of PKA in the present model, and the activity was calculated with a K_d of 2.9 μM (Hill coefficient, n_H = 1.4) determined by Dao et al. (9). Distinct values of $K_{1/2}$ were reported for Epac1 and 2 [30 μM for Epac1 (20) and 20 μM for Epac2 (52, 63)], and thus the active fractions were separately determined.

RESULTS

[cAMP] in pancreatic β-cells under resting conditions and GLP-1 stimulation. The basal level of [cAMP] was 1.6 μM at 100 nM [Ca^{2+}] and 1.4 μM at 500 nM [Ca^{2+}] in our model simulation (Table 1). These values of [cAMP] are comparable to 3.4 and 3.2 μM measured in rat primary β-cells at 1.4 and 20 mM [glucose], respectively (11). Upon stimulation with 10 nM GLP-1 for 15 min, [cAMP] increased to 4.2 μM at 100 nM [Ca^{2+}] and to 5.6 μM at 500 nM [Ca^{2+}] in our model. If PDE was inhibited by 80% (corresponding to 250 μM IBMX) in the absence of GLP-1, [cAMP] increased to ~11 μM independently of [Ca^{2+}] levels. These results also agreed well with the experimental observations. When stimulated with 10 nM GLP-1 in the presence of IBMX, [cAMP] elevated to 37.0 μM at 100 nM [Ca^{2+}] and further to 57.6 μM at 500 nM [Ca^{2+}], similarly to the experimental records of 38.2 and 55.2 μM obtained at the low (1.4 mM) and high (20 mM) [glucose], respectively.

The experimental time course of [cAMP] accumulation induced by GLP-1 (66) was also examined (Fig. 3). Upon stimulation with GLP-1 at 25 mM [glucose] in the presence of IBMX, [cAMP] increased rapidly and slowly declined after reaching peaks within 4 min (filled circles, Fig. 3*A*). The time course of [cAMP] was well reconstructed by simulation at 20% PDE activity and 500 nM [Ca^{2+}] (black curve, Fig. 3*A*). The velocity of cAMP degradation by PDE gradually increases with increasing [cAMP], and the peak is attained when the production rate of cAMP (V_{AC_t}) matched the degradation rate by PDE (V_{PDE} in *Eq. 8*). Simulations revealed that the time to peak as well as the subsequent slow decline in [cAMP] were also influenced by desensitization of the GLP-1 receptor, predominantly due to the state transition to R_{D1} (Fig. 1). In the absence of IBMX, the balance between AC and PDE activities are attained at a much lower [cAMP], thereby giving a time to peak of <1 min (gray curve, Fig. 3*A*). The simulation result was also in good agreement with experimental data (open circles, Fig. 3*A*).

The experimental dose-response relationship obtained by Widmann and colleagues (66) was reconstructed by calculating the [cAMP] accumulation attained over 10 min application of different concentrations of GLP-1 at 20% PDE activity and 500 nM [Ca^{2+}] (Fig. 3, *B* and *C*). At 0.001 and 0.01 nM [GLP-1], [cAMP] increased to a stable saturation level within 2 min (Fig. 3*B*), whereas at higher [GLP-1], the time to peak was delayed with increasing [GLP-1] and the desensitization became more pronounced. As [GLP-1] increases, the activation of V_{AC_G} (see *Eqs. 9~11*) became significant when [GLP-1] >

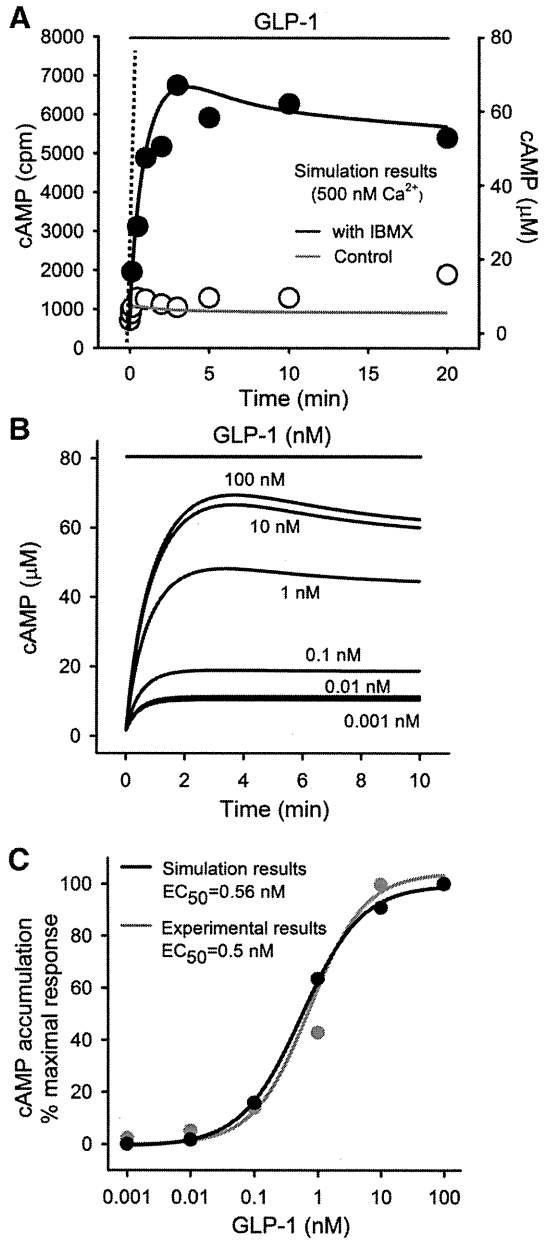

Fig. 3. Time courses of [cAMP] change induced by applying 100 nM GLP-1 (indicated by a horizontal line at the top). *A*: open circles (control) and filled circles [with 1 mM 3-isobutyl-1-methylxanthine (IBMX)] are reproduction of experimental data (66) obtained at 25 mM [glucose] in INS-1 cells. For conversion of units on the left to right vertical axes, see the legend of Table 1. The black and gray curves are simulation results at 500 nM [Ca^{2+}] with and without IBMX, respectively. A 20% activity of PDE was assumed in the presence of IBMX. The dotted line was fitted to the initial rate of rise of [cAMP] to determine the activity of adenylate cyclase (AC). *B*: simulated time courses of the dose-dependent [cAMP] accumulation at 500 nM [Ca^{2+}] during continuous GLP-1 stimulation under the presumptive presence of IBMX (PDE activity inhibited by 80%). *C*: [cAMP] responses to 10 min stimulation with GLP-1 expressed as the percentage of the maximal response in simulation (black line). The dose-response curve was compared with that measured in INS-1 cells (grey line) (66).

0.1 nM and nearly saturated at [GLP-1] slightly larger than 10 nM. In Fig. 3*C*, the dose-dependent accumulation of cAMP at the end of 10 min application of different concentrations of GLP-1 are compared between the simulation and experimental

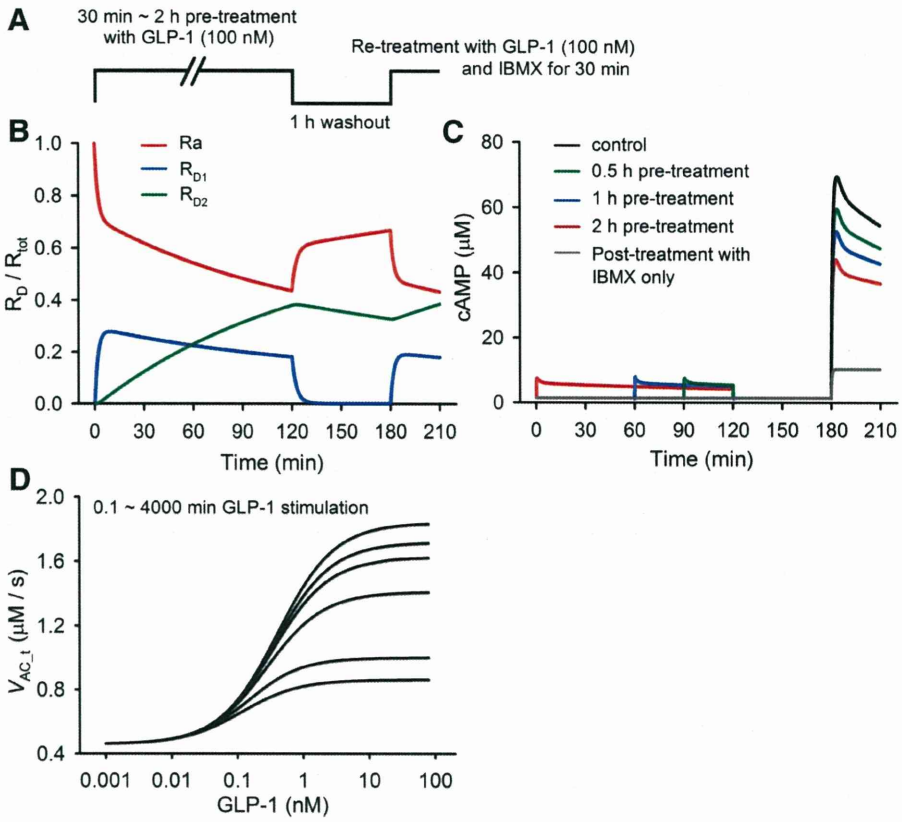

Fig. 4. GLP-1 receptor desensitization. *A*: protocol used in the experimental study of receptor desensitization (3). GLP-1 at 100 nM was applied for various conditioning periods of 30 min to 2 h followed by a 1-h pause before the test application of the same dose. IBMX was only applied with the second application of GLP-1. *B*: time course of the probability of R_a (red) and those of R_{D1} (blue) and R_{D2} (green) in response to the 2-h pretreatment protocol. *C*: [cAMP] response (at 500 nM $[Ca^{2+}]$) to the experimental protocol with varying pretreatment periods, indicated by different colors. The gray trace was obtained by applying IBMX only at the time point of 180 min. *D*: [GLP-1] − V_{AC_t} relations at the end of different stimulation periods of 6 s, 10 s, and 1, 2, 20, 200, 2,000, and 4,000 min, from *top* to *bottom* of 8 curves, respectively. The traces of 6 and 10 s stimulation almost overlapped with one another, indicating that the desensitization was invisible with these short periods, whereas traces with 2,000 and 4,000 min stimulation also overlapped, indicating saturation of the desensitization already at ~2,000 min.

results in INS-1 cells. The half-maximal [GLP-1] is 0.56 nM in the simulation, which is only slightly larger than that obtained in INS-1 cells (0.50 nM).

Ultra-slow desensitization of the GLP-1 receptor. The simulation analysis suggested that the gradual decay of [cAMP] after the peak (Fig. 3, *A* and *B*) during GLP-1 stimulation largely reflects desensitization of the ligand-bound receptor (LR and LRG in Fig. 1) to R_{D1}. However, the R_{D1} kinetics alone failed to reconstruct the very slow inactivation remaining 1 h after washing out agonist as observed by Baggio and colleagues (3). The model including an R_{D2} state in series with R_{D1} reconstructed well the desensitization phenomenon in response to the experimental protocol (Fig. 4*A*). When the 2-h prestimulation protocol was applied (Fig. 4*B*), the R_{D1} fraction (blue curve) increased to a maximum of ~0.28 at the expense of the active fraction (R_a, red curve) within the initial 10 min, and then both R_a and R_{D1} slowly declined thereafter due to a continuous transition to R_{D2} (green curve). During the washout period, the R_{D1} fraction quickly became insignificant, whereas 85% of R_{D2} remained even after 1 h washout. The result suggests that the fraction of R_a available for the second application of GLP-1 decreases depending on the preincubation period. Figure 4*C* shows the [cAMP] response to the experimental protocol with varying pretreatment periods. It is evident, as predicted, that the longer the preincubation period, the more the [cAMP] response was reduced on the second application of GLP-1. The reductions (in %) in [cAMP] accumulations on the second stimulus were normalized to the control amplitude and were summarized in Table 2. These results agreed well with the experimental observations (3).

To characterize the steady-state desensitization of the GLP-1 receptor, the [GLP-1]-dependent V_{AC_t} at varying incubation periods (10 s ~ 4,000 min) were computed over the range 0.001~100 nM [GLP-1] (Fig. 4*D*). With 6- and 10-s applications, V_{AC_t} nearly overlap one another virtually without any sign of receptor desensitization. When the duration of GLP-1 application was prolonged, the desensitization gradually developed and a steady state was obtained at ~2,000 min application, which gave ~25% of the control V_{AC_t} at the saturating [GLP-1]. The extent of desensitization was more pronounced when stimulated with higher [GLP-1].

Cross-talk between glucose and GLP-1 signal pathways in determining [cAMP]. Experimental studies in Min6 and INS-1 β-cells demonstrated that [cAMP] increased in phase with a temporal increase in $[Ca^{2+}]$ in the presence of GLP-1, whereas

Table 2. *Reduction of GLP-1-dependent [cAMP] accumulation induced by prestimulation of receptors for different time periods*

	Preincubation Period With 100 nM GLP-1		
	0.5 h	1 h	2 h
% Reduction			
Simulation results	16	26	40
Experimental results	21	35	50

The [cAMP] accumulation caused by IBMX alone (Fig. 4*C*) was subtracted from the [cAMP] responses to the second application of agonist, and the differences were normalized to the control value. The simulation results are compared with the experimental data in INS-1 cells (3). See text for definitions of abbreviations.

the relation between [cAMP] and [Ca^{2+}] was out of phase without agonist (19, 23, 38). The simulation in Fig. 5 examines mechanisms of [Ca^{2+}]-dependent regulation of [cAMP] in the absence or presence of GLP-1. In the absence of GLP-1, the total cAMP production rates V_{AC_t} (V_{AC} + V_{AC_G}) matched the V_{PDE} at a resting [cAMP] of 1.6 μM (black curve in Fig. 5*A*) at 100 nM [Ca^{2+}]. When [Ca^{2+}] was increased to 500 nM (grey curve), [cAMP] slightly decreased to 1.4 μM due to the facilitation of PDE activity by [Ca^{2+}] (V_{Cd_PDE}, grey curve in Fig. 5*C*). After 30 min simulation with 100 nM [GLP-1], [cAMP] increased to 4.1 μM (Fig. 5*B*) due to enhanced V_{AC_G} at 100 nM [Ca^{2+}]. Increasing [Ca^{2+}] to 500 nM further elevated [cAMP] in a reversible manner up to 5.4 μM because the activation of AC_G by [Ca^{2+}] (V_{Cd_AC}, black curve in Fig. 5*D*) was relatively larger than that of PDE (V_{Cd_PDE}). These simulation results revealed the mechanisms underlying the in-phase or out-of-phase patterns of [cAMP] fluctuations in response to the cyclic changes in [Ca^{2+}] (19, 23, 38). To get a deeper insight into the physiological significance of [Ca^{2+}] in determining [cAMP], the changes in [cAMP] in response to increasing [Ca^{2+}] from 0.05 to 5.0 μM were simulated at varying [GLP-1]. The depression of [cAMP] response induced by increasing [Ca^{2+}] at a lower [GLP-1] was inverted at ~0.054 nM [GLP-1], and the enhancement of [cAMP] synthesis by [Ca^{2+}] was augmented further with increasing [GLP-1], saturating at ~2 μM [Ca^{2+}] (Fig. 5*E*). Note that with higher [Ca^{2+}] (≳5 μM), cAMP response to GLP-1 starts to decrease, reflecting the [Ca^{2+}]-dependent inactivation (see *Eq. 11*).

Activation of PKA and Epac by GLP-1. Time courses of [cAMP] responses to GLP-1 were measured using a PKA-based biosensor in INS-1 cells (19). The fluorescent signals were detected using evanescent wave microscopy reflecting [cAMP] in the submembrane space. However, since the signals were not calibrated, extent of PKA activation by the GLP-1 stimulus was not obtained from the experimental results. We thus attempted to predict PKA activity using the GLP-1 receptor signal cascade model developed in the present study (Fig. 6). Toward this end, it was essential to examine the localization of cAMP under the surface membrane compared with the bulk [cAMP], since the PKA activities may vary within the cytosol due to an uneven distribution of cAMP. In pancreatic β-cells, highly localized cAMP microdomain may possibly be present

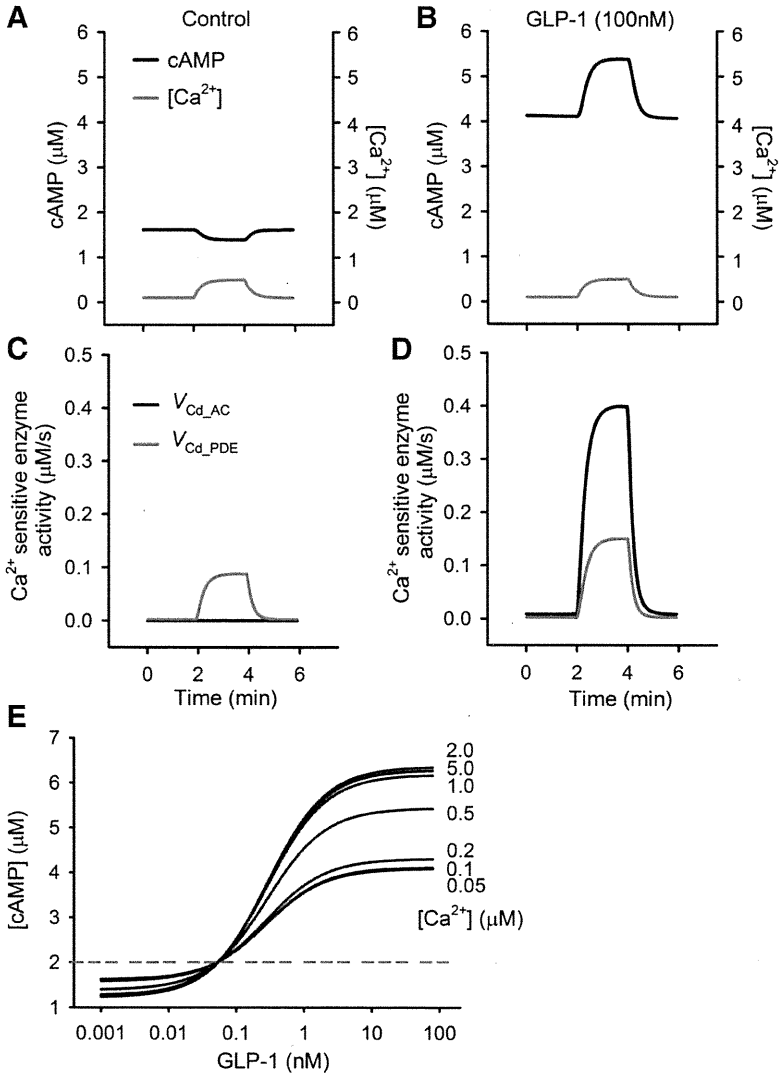

Fig. 5. [cAMP] responses to changes in [Ca^{2+}]. *A* and *B*: [Ca^{2+}] (gray lines) was varied from 100 to 500 nM with a time constant of 30 s in the absence (*A*) or presence (*B*) of 100 nM GLP-1. [cAMP] (black lines) responses to the corresponding [Ca^{2+}]. *C* and *D*: [Ca^{2+}]-dependent AC_G (V_{Cd_AC}, black line) and PDE (V_{Cd_PDE}, grey line) activities under the conditions examined in *A* and *B*, respectively. *E*: [GLP-1]-[cAMP] response curves at varying [Ca^{2+}] (0.05, 0.1, 0.2, 0.5, 1.0, 2.0, and 5.0 μM). Dotted gray line indicates [cAMP] at [GLP-1] = 0.054 nM, where decreasing [cAMP] responses to increasing [Ca^{2+}] at a lower [GLP-1] is converted to increasing [cAMP].

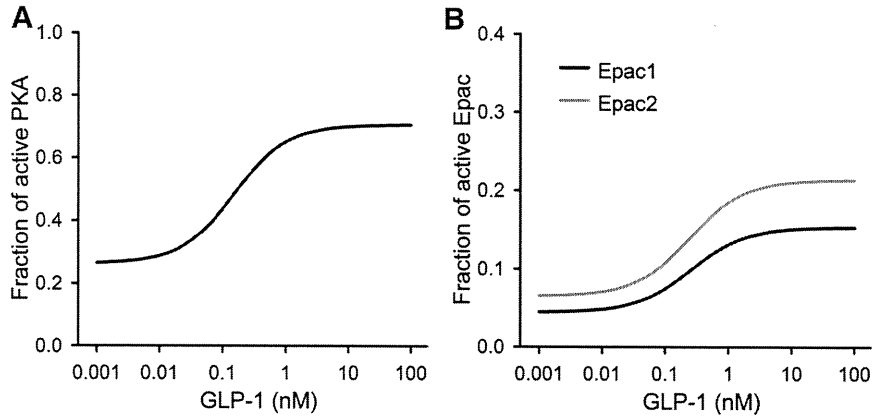

Fig. 6. Dose-dependent activities of protein kinase A (PKA) and exchange protein directly activated by cAMP (Epac) at 500 nM [Ca^{2+}] after 30 min stimulation with various concentrations of GLP-1. *A*: fraction of active PKA. *B*: fractions of active Epac1 (black line) and 2 (grey line).

at submembrane space, since production of cAMP by ACs is limited at the surface membrane (29, 38), while PDE-mediated degradation occurs diffusely within the cytosol (4, 54). Indeed, cAMP microdomain has been observed beneath the surface membrane in other cell types, such as cardiac myocytes (70) and HEK cells (61).

To simulate the distribution of [cAMP], intracellular diffusion of cAMP was calculated (Fig. 7). For simplicity, one-dimensional diffusion was assumed over a distance of 4 μm (estimated from Ref. 48) from the surface membrane toward the nucleus as indicated in Fig. 7*A*. The diffusion path (x) was separated into 200 compartments, and [cAMP] in each compartment at time t [C (x,t)] was calculated using the following equation:

$$\frac{\partial C(x,t)}{\partial t} = D \cdot \frac{\partial^2 C(x,t)}{\partial x^2} \qquad (14)$$

With boundary condition of

$$\left.\frac{\partial C}{\partial x}\right|_{x=0,4} = 0$$

where the diffusion coefficient (D) was 0.3 μm^2/ms based on experimental measurements of 0.27 μm^2/ms (6) and 0.33 μm^2/ms (32). The cAMP production by AC stimulated by a [GLP-1] of 10 nM was assumed only in the first compartment (29, 38), whereas cAMP degradation by PDE was calculated in all compartments (4, 54). A quasi-steady-state concentration gradient of [cAMP] was established within 100 ms after the onset of AC activation, and the difference in [cAMP] over the diffusion path of 4 μm was only about 0.05 μM. Theoretically, but unrealistically, a much larger gradient (4 μM) was developed only when V_{PDE} was increased by 100 times. The distributions of [cAMP] relative to [cAMP] in the submembrane space simulated using the control and high V_{PDE} are shown in Fig. 7, *B* and *C*, respectively. This finding agrees with simulation results demonstrated by Oliveira et al. (47) (see DISCUSSION for more detail). The flat distribution in Fig. 7*B* may justify the use of average [cAMP] in estimation of active fractions of cAMP effecters that are distributed throughout the cytosol of pancreatic β-cells.

With the use of the GLP-1 receptor signal transduction model, the dose-dependent activities of PKA at the end of 30 min application of various concentrations (0.001~100 nM) of GLP-1 under high [Ca^{2+}] condition were simulated (Fig. 6*A*). The [cAMP]-dependent PKA activation was calculated using a

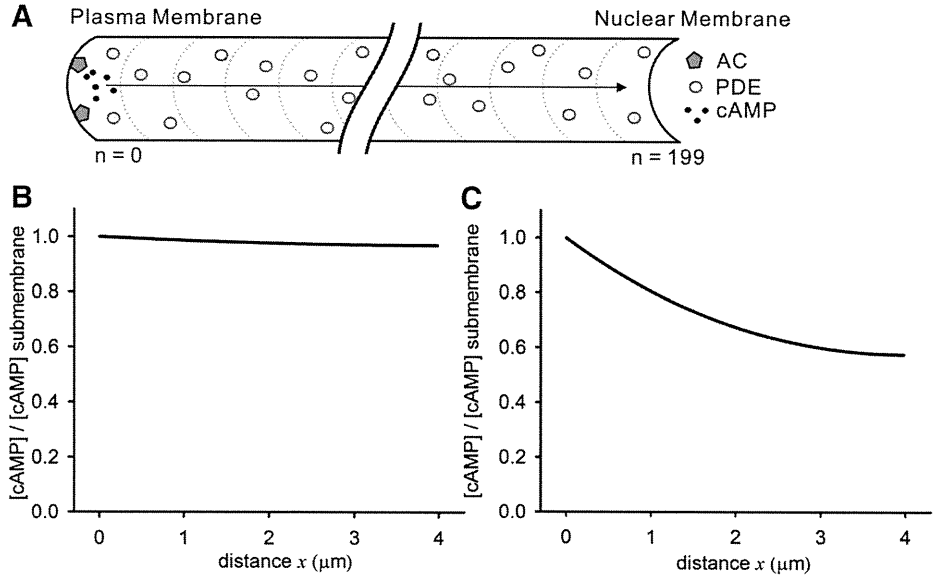

Fig. 7. [cAMP] gradient in the cytosol of a pancreatic β-cell during GLP-1 stimulation. *A*: one-dimensional diffusion of cAMP (arrow) was assumed from the surface membrane (*left*) toward the nuclear membrane (*right*) over a distance of 4 μm. The diffusion path was separated into 200 compartments, and AC activity was included only in the first compartment, while a homogeneous PDE distribution was assumed in all compartments. V_{AC} and V_{PDE} under 10 nM GLP-1 stimulation at 500 nM [Ca^{2+}] were applied for the calculation. *B*: gradient of [cAMP] over the distance of diffusion path in a pancreatic β-cell. *C*: [cAMP] gradient obtained with the same experimental conditions as in *B* except V_{max_PDE} was multiplied by 100.

K_d and nH (see APPENDIX I) obtained by Dao et al. (9). A significant fraction (~26%) of PKA was already active under the control condition of 1.4 μM [cAMP] at 500 nM [Ca^{2+}] without GLP-1 stimulation. As shown in Fig. 6*A*, the activity of the enzyme dose dependently increased, and the application of 100 nM [GLP-1] induced nearly the saturating activation of PKA (~70%) through an increase in [cAMP] to 5.4 μM. With the same experimental conditions as in Fig. 6*A*, the active fractions of Epac1 and 2, other cAMP effectors, were also simulated using the half-maximal values of cAMP for the activation of each enzyme (APPENDIX I). GLP-1 at 100 nM activates Epac1 from 4.4% of basal activity to 15.3%, whereas active Epac2 was about 6.4% at rest and was increased to ~21.3% (Fig. 6*B*).

Systems analysis on the balance between the production and degradation of cAMP. The level of [cAMP] is determined by the balance between AC and PDE activities (*Eq. 8*). Depression of V_{PDE} below V_{AC} will cause collapse of [cAMP] regulation, leading to a continuous accumulation of cAMP within cytosol. In both experiments and computer model simulations, quasi-steady-state [cAMP] levels were obtained even when the PDE activity was depressed by a saturating dose (>200 μM) of [IBMX]. This is because balancing V_{AC_t} with V_{PDE} was established with the IBMX-insensitive PDE fraction (~20% total PDE activities) under this extreme condition. To examine the robustness of the [cAMP] homeostasis in our model, the V_{AC_t} devoid of desensitization was compared with V_{PDE}, and the steady-state level of [cAMP] was defined by the intersection of V_{AC_t} with the [cAMP]-V_{PDE} curve in Fig. 8. When the V_{AC_t} was maximized at 500 nM [Ca^{2+}] using the saturating concentration of 100 nM [GLP-1], the equilibrium [cAMP] was obtained at ~115.7 μM with 20% V_{PDE} (grey sigmoidal curve) as indicated by the *arrow a*. This analysis determines that depression of V_{PDE} below ~14% will cause collapse of the [cAMP] homeostasis when V_{AC_t} was maximized. Under physiological conditions, the steady-state [cAMP] was maintained at 7.9 μM (*arrow b*) with intact V_{PDE} (black sigmoidal curve) even when AC was fully activated. The lower limit of [cAMP] in the absence of GLP-1 stimulation, on the other hand, is determined by the activity of the G protein-insensitive component of AC, and the [cAMP] was balanced at 1.4 μM (*arrow c*). It should be noted that this range of [cAMP] change (1.4~7.9 μM) well fits the dynamic range of the PKA activation ($K_{1/2}$ = ~3 μM). This analysis revealed that the intact PDE is highly capable of balancing V_{AC_t}, and thus we conclude that the system of [cAMP] regulation is quite robust in pancreatic β-cells. The delayed desensitization of the GLP-1 receptor (Fig. 4*D*) may further strengthen the robustness of the system.

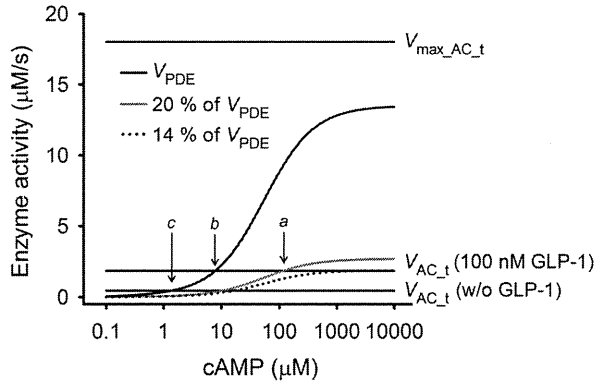

Fig. 8. Systems analysis on the robustness of GLP-1 signaling system in [cAMP] regulation. The black sigmoidal curve, the control V_{PDE} plotted as a function of [cAMP] at 500 nM [Ca^{2+}] (see *Eq. 13*). Grey curve, 20% of V_{PDE} under the presumptive presence of IBMX. Dotted curve, 14% V_{PDE}. The three horizontal lines from *top* to *bottom* indicate the sum of (V_{max_AC} + $V_{max\_AC\_G}$) and two levels of V_{AC_t} at 100 nM and 0 [GLP-1], respectively. To evaluate maximum possible levels of [cAMP] increase, the desensitization of the receptor was removed in this calculation. The *arrows a*, *b*, and *c* indicate intersections of V_{PDE} and V_{AC} curves. Note that [cAMP] can vary between the minimum level given by the *arrow c* and the maximum level given by the *arrow b* under the physiological condition. With 20% V_{PDE}, [cAMP] could increase to an extreme level (*arrow a*). Inhibition of V_{PDE} exceeding 14% would causes the "break-down" of the signaling system leading to a continuous [cAMP] accumulation, indicating that the intact PDE has an excessive capacity to balance against the production of cAMP by AC under physiological condition.

DISCUSSION

In the present study, a minimal model of GLP-1 receptor signal transduction was developed mostly based on experimental data reported in β-cells or related cell lines. The model successfully reconstructed the experimental findings of dynamic changes in [cAMP] during agonist stimulation in the absence or presence of IBMX at two representative levels of [Ca^{2+}] (Fig. 3). The model predicted the activity of cAMP effectors PKA and Epac during GLP-1 stimulation (Fig. 6). The simulation also demonstrated that the GLP-1 receptor desensitization kinetics applied to the model successfully explained the fast and very slow inactivation steps, which have significant effects on the decay kinetics of [cAMP] during continuous GLP-1 stimulation (Fig. 3) as well as reduced [cAMP] production after preconditioning of the receptor (Fig. 4 and Table 2). The cross talk between glucose- and GLP-1-dependent signal cascades in synergistic synthesis of cAMP was well reconstructed by incorporating the direct regulation of both AC and PDE by [Ca^{2+}] (Table 1). Models of the [Ca^{2+}]-dependent AC and PDE activities also elucidated the fractions of [Ca^{2+}]-sensitive components of these enzymes. Considering that [Ca^{2+}] is raised by [glucose] stimulation via the enhanced electrical activity of β-cells, the activation of GLP-1 signaling is a powerful amplifier for promoting the insulin release in the presence of stimulating concentrations of glucose.

The insulinotropic effect of the cAMP signal involves the activation of PKA and Epac, and subsequent modulation of ion channel functions (26, 31, 35, 41, 42, 57) and Ca^{2+} release from ER (27, 36, 64), in addition to their direct effects on the exocytotic machinery. The effects on ion channels, for example, include the enhancement of Ca^{2+} influx via L-type Ca^{2+} currents (26, 57) and inhibition of K^+ currents (26, 31, 35, 41, 42), which may in turn promote the insulin release via an increase in the membrane excitability. These comprehensive mechanisms of the insulinotropic effect of GLP-1 will be analyzed by incorporating the GLP-1 receptor signaling cascade model into appropriate whole β-cell models (24, 44) in the future.

In the present study, the distribution of [cAMP] within the cytosol of pancreatic β-cells was estimated (Fig. 7). It was suggested that the localization of cAMP beneath the surface membrane is insignificant even though production of cAMP is

limited at the submembrane space, while PDE-mediated degradation occurs diffusely within the cytosol. Our finding is, however, different from the localized cAMP microdomain observed in other cell types [cardiac myocytes (70) and HEK293 cells (61)]. The theoretical study by Oliveira et al. (47) demonstrated a large [cAMP] gradient (~5 μM) in HEK293 cells upon stimulation with PGE1. They concluded that the PDE4D activity enhanced by PKA-mediated phosphorylation was necessary and sufficient for generating the cAMP microdomain observed by Terrin et al. (61), and no physical barrier was required against the cAMP diffusion. If compared with our simulation, the cAMP diffusion constant used in their study was essentially the same magnitude as in our calculations. Interestingly, our diffusion model also generated a similar [cAMP] gradient of ~4 μM (Fig. 7*C*) when simulated using the V_{PDE} equivalent to that used in the Oliveira et al. (47). However, their V_{PDE} was much higher (~100 hold) than that determined by the model fitting to the published experimental data in the present study. If we adopt the higher PDE activity, the model failed to reconstruct experimental records of [cAMP] changes during GLP-1 stimulation. Our simulation results strongly suggest that the distribution of cAMP is homogeneous in pancreatic β-cells because of relatively low PDE activities. These results, however, do not necessarily exclude the possibility of a functional coupling among AC, PKA, and/or Epac and effecter proteins by AKAP near the membrane, which has been suggested in the heart and brain (12, 46). On the other hand, the rapid diffusion of [cAMP] could possibly be an essential factor in the GLP-1 receptor signaling for a proper modulation of insulin release, since PKA and Epac, the target proteins of cAMP, are widely distributed throughout the intracellular space (12, 40, 49). For activation of all these enzymes, the rapid access of cAMP might be critical to fulfill the basic needs of subsequent modulatory actions on ion channels on the surface and ER membrane as well as exocytotic machinery in concert within the entire intracellular space.

Sensitivity of the model to varying parameters. Athough [R] was estimated in a previous study (66), [G] has not yet been determined in pancreatic β-cells. In the present study, [G] was referred by Post et al. (50), who suggested the expression of G_s protein in large excess relative to β-adrenergic receptor in cardiac myocytes and hypothesized that this stoichiometry of [G] to [R] will be applicable to other G protein-coupled hormone receptor systems. We found that the EC_{50} of [GLP-1]-dependent [cAMP] accumulation is dependent on the agonist-induced [LRG] complex ([LRG] = [G]·[LR]/K_d), and thereby the EC_{50} can be adjusted by modifying either [G] or K_d of [G]-[LR] binding. Since both parameters have not been investigated in pancreatic β-cells, [GLP-1]-dependent [cAMP] accumulation was reconstructed by determining an appropreate K_d in the present study under the assumption that [G] is expressed to a similar extent as in the cardiac tissue (50). The fraction of [R_a] is one of signaling factors that have the strong influence on AC activities and thus [cAMP]. Under physiological conditions, [R_a] will largely fluctuate because of extensive desensitization (75% at the maximum, see Fig. 4*D*), which is expected to proceed during several hours of the meal digestion.

The maximum AC activity ($V_{max\_AC\_t} = V_{max\_AC} + V_{max\_AC\_G}$) is much larger than the V_{max} of PDE in our model. The lower AC activity under physiological conditions is mostly due to the low sensitivity of AC to G_αGTP in addition to the low [G_αGTP] production, even with a saturating [GLP-1] (see *Eq. 11*). Other modulatory factors of the AC activity, such as the dependencies on the substrate ATP and the Ca^{2+}-dependent inactivation, are nearly saturated with the physiological level of [ATP] and [Ca^{2+}]. Although Ca_xCaM-dependent activation of V_{AC_G} is pronounced with increasing [GLP-1], [cAMP] production becomes partially compensated by the parallel activation of PDE. More specifically, [cAMP] level balances at 7.61 μM under the stimulation with 10 nM GLP-1 at 500 nM [Ca^{2+}] without desensitization processes, whereas it increased to 8.61 μM when the component of Ca_xCaM-dependent activation of V_{PDE} was excluded from the model. The PDE component showing the high cAMP sensitivity (K_{mL}) also plays a subtle role in regulation [cAMP], whereas the low cAMP sensitivity (K_{mH}) component virtually fulfills the physiological role in cAMP hydrolysis in the present model.

Limitations. The kinetics of the simple sequential transition of desensitized receptors from R_{D1} to R_{D2} was modeled to describe the time course of the delayed recovery from slow inactivation (Fig. 4). Indeed, the reaction scheme for receptor desensitization (Fig. 1) well simulated both of the fast and very slow desensitization observed in experimental studies (see RESULTS). Up to date, it is clear that the phosphorylation of the GLP-1 receptor is the key desensitization step, whereas Widmann and colleagues (67) have shown that neither PKA nor PKC are involved in the process. The involvement of β-Arrestin2 and GRK5 was suggested by Jorgensen et al. (34), whereas it is still highly controversial since a different group demonstrated the desensitization was independent of β-Arrestin2 (59). The model scheme will need to be improved when the molecular mechanisms are established in future experimental studies. It may also be examined whether the activation of PDE through phosphorylation by PKA is responsible for a small fraction of the spontaneous decay of [cAMP], although the present study attributed the decay only to desensitization.

The active fractions of PKA as well as Epac1 and 2 were calculated by a use of biochemically determined K_d or $K_{1/2}$, half-maximal [cAMP] for the activation of these enzymes. However, especially for PKA activation, there has been obvious disagreement in published values of $K_{1/2}$, which vary over a nanomolar to micromolar range. It seems that the experimental $K_{1/2}$ is highly related to the concentration of enzyme used in biochemical investigations (7). $K_{1/2}$ was ~3 μM for more physiological concentration of the PKA isozyme II (400 nM), whereas it was significantly reduced to ~50 nM when tested on 1 nM holoenzyme. Indeed, other investigators (14) used low holoenzyme concentrations of 20~30 nM and obtained a $K_{1/2}$ of 98 nM and 540 nM for PKAI and PKAII, respectively. In the present study, PKA activities were calculated with $K_{1/2}$ of ~3 μM, yet, it may need to be reevaluated when more accurate experimental measurements of $K_{1/2}$ values as well as concentrations of PKA isozyme become available.

cAMP is distributed within a β-cell in forms of free cAMP and PKA or Epac-bound form (cAMP-PKA and cAMP-Epac). In the present study, however, [cAMP] was calculated neglecting [cAMP-PKA] and [cAMP-Epac]. If the total amount of cAMP is comparable to PKA and/or Epac, it will be necessary to consider [PKA] and/or [Epac] in calculating the concentration of unbound cAMP ($[cAMP]_{total}$ = [cAMP] + [cAMP-PKA] + [cAMP-Epac]). Similarly, the mass conservation should also be consid-

ered for [$G_\alpha GTP$] ([$G_\alpha GTP_{total}$] = [$G_\alpha GTP$] + [$G_\alpha GTP$-AC]) when [AC] is available. Since the amounts of PKA, Epac, and AC are not determined in β-cells, we excluded these conservation equations from the present model.

APPENDIX I

A) Parameters Determined in Published Experimental Studies

1) Parameters determined based on GLP-1 signaling system in pancreatic β-cell and a β-cell line

Total amount of receptor, [R_t] 0.00434 μM (Ref. 66)

Binding between [L] and [R] K_d = 0.004 μM (Refs. 43, 65)

2) Parameters determined by biochemical investigations

Total amount of Gs, [G_t] 2.83 μM (Ref. 50)

$G_\alpha GTP_{tot}$-dependent AC_G activation $K_{1/2}$ = 0.4 μM (Ref. 58)

ATP-dependent AC activity K_m = 1.03 mM (Ref. 13)

ATP-dependent AC_G activity K_m = 0.315 mM (Ref. 13)

Ca_xCaM-dependent AC_G activation $K_{1/2}$ = 0.348 μM (Ref. 21)

Ca^{2+}-dependent AC_G inhibition $K_{1/2i}$ = 75 μM (Ref. 21)

Ca_xCaM-dependent PDE activation $K_{1/2}$ = 0.348 μM (Ref. 68)

cAMP-dependent PKA activation K_d = 2.9μM,n_H = 1.4 (Ref.9)

cAMP-dependent Epac1 activation $K_{1/2}$ = 30 μM (Ref. 20)

cAMP-dependent Epac2 activation $K_{1/2}$ = 20 μM (Refs. 52, 63)

The kinetics for the activation and deactivation of Gs protein

$k5$ = 16 s-1, $k6$ = 1 s-1, $k7$ = 1, 200, 000 mM/s (Refs. 5, 56)

B) Parameters Determined in the Present Study by Fitting Specific Experimental Records or Measurements in References

Desensitization rate constants

$k1$ = 0.0025 s-1, $k2$ = 0.005833 s-1 (Fig. 3)

$k3$ = 0.0002833 s-1, $k4$ = 0.00005 s-1 (Fig. 4 and Table 3)

AC and PDE activities (Figs. 3 and 6 and Table 2)

$$V_{AC}V_{max\_AC} = 0.0006173 \text{ mM/s}$$

$$V_{AC\_G}V_{max\_AC\_G} = 0.01738 \text{ mM/s}$$

$$f_{Cd\_AC} = 0.6$$

V_{PDE}

$$V_{max\_PDE} = 0.015 \text{ mM/s}$$

$$f_{Cd\_PDE} = 0.2$$

$$K_{ml} = 0.4148 \text{ μM}, K_{mH} = 53.98 \text{ μM}$$

$$f = 0.012$$

C) Parameters Determined in the Present Study by Fitting the Overall Model Scheme to Experimental Records or Measurements In References

Binding between [G] and [LR] K_d = 0.372 μM (Ref. 66)

ACKNOWLEDGMENTS

The authors acknowledge insightful discussions with Dr. T. Powell and valuable suggestions made by Dr. G. G. Holz. The authors also thank Drs. T. Shimayoshi, C. Cha, Y. Himeno, and other members in the Biosimulation Project for helpful discussion as well as technical supports.

GRANTS

This work was supported by the Regional Innovation Cluster Program (Biomedical Cluster Kansai) of the Ministry of Education, Culture, Sports, Science and Technology, Japan and a Grant-In-Aid for Scientific Research from the Ministry of Education, Culture, Sports, Science and Technology, Japan.

DISCLOSURES

No conflicts of interest, financial or otherwise, are declared by the author(s).

REFERENCES

1. **Ahmad M, Abdel-Wahab YH, Tate R, Flatt PR, Pyne NJ, Furman BL.** Effect of type-selective inhibitors on cyclic nucleotide phosphodiesterase activity and insulin secretion in the clonal insulin secreting cell line BRIN-BD11. *Br J Pharmacol* 129: 1228–1234, 2000.
2. **Arava Y, Adamsky K, Ezerzer C, Ablamunits V, Walker MD.** Specific gene expression in pancreatic beta-cells: cloning and characterization of differentially expressed genes. *Diabetes* 48: 552–556, 1999.
3. **Baggio LL, Kim JG, Drucker DJ.** Chronic exposure to GLP-1R agonists promotes homologous GLP-1 receptor desensitization in vitro but does not attenuate GLP-1R-dependent glucose homeostasis in vivo. *Diabetes* 53, *Suppl* 3: S205–S214, 2004.
4. **Bender AT, Beavo JA.** Cyclic nucleotide phosphodiesterases: molecular regulation to clinical use. *Pharmacol Rev* 58: 488–520, 2006.
5. **Brandt DR, Ross EM.** Catecholamine-stimulated GTPase cycle. Multiple sites of regulation by beta-adrenergic receptor and Mg^{2+} studied in reconstituted receptor-Gs vesicles. *J Biol Chem* 261: 1656–1664, 1986.
6. **Chen C, Nakamura T, Koutalos Y.** Cyclic AMP diffusion coefficient in frog olfactory cilia. *Biophys J* 76: 2861–2867, 1999.
7. **Christensen AE, Selheim F, de RJ, Dremier S, Schwede F, Dao KK, Martinez A, Maenhaut C, Bos JL, Genieser HG, Doskeland SO.** cAMP analog mapping of Epac1 and cAMP kinase. Discriminating analogs demonstrate that Epac and cAMP kinase act synergistically to promote PC-12 cell neurite extension. *J Biol Chem* 278: 35394–35402, 2003.
8. **Cooper DM.** Regulation and organization of adenylyl cyclases and cAMP. *Biochem J* 375: 517–529, 2003.
9. **Dao KK, Teigen K, Kopperud R, Hodneland E, Schwede F, Christensen AE, Martinez A, Doskeland SO.** Epac1 and cAMP-dependent protein kinase holoenzyme have similar cAMP affinity, but their cAMP domains have distinct structural features and cyclic nucleotide recognition. *J Biol Chem* 281: 21500–21511, 2006.
10. **Dean PM.** Ultrastructural morphometry of the pancreatic cell. *Diabetologia* 9: 115–119, 1973.
11. **Delmeire D, Flamez D, Hinke SA, Cali JJ, Pipeleers D, Schuit F.** Type VIII adenylyl cyclase in rat beta cells: coincidence signal detector/generator for glucose and GLP-1. *Diabetologia* 46: 1383–1393, 2003.
12. **Dessauer CW.** Adenylyl cyclase–A-kinase anchoring protein complexes: the next dimension in cAMP signaling. *Mol Pharmacol* 76: 935–941, 2009.
13. **Dessauer CW, Scully TT, Gilman AG.** Interactions of forskolin and ATP with the cytosolic domains of mammalian adenylyl cyclase. *J Biol Chem* 272: 22272–22277, 1997.
14. **Dostmann WR, Taylor SS.** Identifying the molecular switches that determine whether (Rp)-cAMPS functions as an antagonist or an agonist in the activation of cAMP-dependent protein kinase I. *Biochemistry* 30: 8710–8716, 1991.
15. **Dov A, Abramovitch E, Warwar N, Nesher R.** Diminished phosphodiesterase-8B potentiates biphasic insulin response to glucose. *Endocrinology* 149: 741–748, 2008.
16. **Drucker DJ.** The biology of incretin hormones. *Cell Metab* 3: 153–165, 2006.
17. **Drucker DJ, Philippe J, Mojsov S, Chick WL, Habener JF.** Glucagon-like peptide I stimulates insulin gene expression and increases cyclic AMP levels in a rat islet cell line. *Proc Natl Acad Sci USA* 84: 3434–3438, 1987.
18. **Dryselius S, Grapengiesser E, Hellman B, Gylfe E.** Voltage-dependent entry and generation of slow Ca^{2+} oscillations in glucose-stimulated pancreatic β-cells. *Am J Physiol Endocrinol Metab* 276: E512–E518, 1999.
19. **Dyachok O, Isakov Y, Sagetorp J, Tengholm A.** Oscillations of cyclic AMP in hormone-stimulated insulin-secreting beta-cells. *Nature* 439: 349–352, 2006.
20. **Enserink JM, Christensen AE, de RJ, van TM, Schwede F, Genieser HG, Doskeland SO, Blank JL, Bos JL.** A novel Epac-specific cAMP

analogue demonstrates independent regulation of Rap1 and ERK. *Nat Cell Biol* 4: 901–906, 2002.

21. **Fagan KA, Mahey R, Cooper DM.** Functional co-localization of transfected Ca(2+)-stimulable adenylyl cyclases with capacitative Ca^{2+} entry sites. *J Biol Chem* 271: 12438–12444, 1996.
22. **Frace AM, Mery PF, Fischmeister R, Hartzell HC.** Rate-limiting steps in the beta-adrenergic stimulation of cardiac calcium current. *J Gen Physiol* 101: 337–353, 1993.
23. **Fridlyand LE, Harbeck MC, Roe MW, Philipson LH.** Regulation of cAMP dynamics by Ca^{2+} and G protein-coupled receptors in the pancreatic β-cell: a computational approach. *Am J Physiol Cell Physiol* 293: C1924–C1933, 2007.
24. **Fridlyand LE, Tamarina N, Philipson LH.** Modeling of Ca^{2+} flux in pancreatic β-cells: role of the plasma membrane and intracellular stores. *Am J Physiol Endocrinol Metab* 285: E138–E154, 2003.
25. **Gilon P, Ravier MA, Jonas JC, Henquin JC.** Control mechanisms of the oscillations of insulin secretion in vitro and in vivo. *Diabetes* 51, *Suppl* 1: S144–S151, 2002.
26. **Gromada J, Bokvist K, Ding WG, Holst JJ, Nielsen JH, Rorsman P.** Glucagon-like peptide 1 (7–36) amide stimulates exocytosis in human pancreatic beta-cells by both proximal and distal regulatory steps in stimulus-secretion coupling. *Diabetes* 47: 57–65, 1998.
27. **Gromada J, Brock B, Schmitz O, Rorsman P.** Glucagon-like peptide-1: regulation of insulin secretion and therapeutic potential. *Basic Clin Pharmacol Toxicol* 95: 252–262, 2004.
28. **Han P, Werber J, Surana M, Fleischer N, Michaeli T.** The calcium/calmodulin-dependent phosphodiesterase PDE1C down-regulates glucose-induced insulin secretion. *J Biol Chem* 274: 22337–22344, 1999.
29. **Hanoune J, Defer N.** Regulation and role of adenylyl cyclase isoforms. *Annu Rev Pharmacol Toxicol* 41: 145–174, 2001.

29a. **Harvey, RD.** How uniform is cAMP signaling? Focus on "Systems analysis of GLP-1 receptor signaling in pancretic β-cells." *Am J Physiol Cell Physiol* (July 20, 2011). doi:10.1152/ajpcell.00245.2011.

30. **Holz GG.** Epac: A new cAMP-binding protein in support of glucagon-like peptide-1 receptor-mediated signal transduction in the pancreatic beta-cell. *Diabetes* 53: 5–13, 2004.
31. **Holz GG, Kuhtreiber WM, Habener JF.** Pancreatic beta-cells are rendered glucose-competent by the insulinotropic hormone glucagon-like peptide-1(7–37). *Nature* 361: 362–365, 1993.
32. **Huang RC, Gillette R.** Kinetic analysis of cAMP-activated Na^+ current in the molluscan neuron. A diffusion-reaction model. *J Gen Physiol* 98: 835–848, 1991.
33. **Idevall-Hagren O, Barg S, Gylfe E, Tengholm A.** cAMP mediators of pulsatile insulin secretion from glucose-stimulated single beta-cells. *J Biol Chem* 285: 23007–23018, 2010.
34. **Jorgensen R, Martini L, Schwartz TW, Elling CE.** Characterization of glucagon-like peptide-1 receptor beta-arrestin 2 interaction: a high-affinity receptor phenotype. *Mol Endocrinol* 19: 812–823, 2005.
35. **Kang G, Chepurny OG, Malester B, Rindler MJ, Rehmann H, Bos JL, Schwede F, Coetzee WA, Holz GG.** cAMP sensor Epac as a determinant of ATP-sensitive potassium channel activity in human pancreatic beta cells and rat INS-1 cells. *J Physiol* 573: 595–609, 2006.
36. **Kang G, Chepurny OG, Rindler MJ, Collis L, Chepurny Z, Li WH, Harbeck M, Roe MW, Holz GG.** A cAMP and Ca^{2+} coincidence detector in support of Ca^{2+}-induced Ca^{2+} release in mouse pancreatic beta cells. *J Physiol* 566: 173–188, 2005.
37. **Kashima Y, Miki T, Shibasaki T, Ozaki N, Miyazaki M, Yano H, Seino S.** Critical role of cAMP-GEFII–Rim2 complex in incretin-potentiated insulin secretion. *J Biol Chem* 276: 46046–46053, 2001.
38. **Landa LR Jr, Harbeck M, Kaihara K, Chepurny O, Kitiphongspattana K, Graf O, Nikolaev VO, Lohse MJ, Holz GG, Roe MW.** Interplay of Ca^{2+} and cAMP signaling in the insulin-secreting MIN6 beta-cell line. *J Biol Chem* 280: 31294–31302, 2005.
39. **Lester LB, Langeberg LK, Scott JD.** Anchoring of protein kinase A facilitates hormone-mediated insulin secretion. *Proc Natl Acad Sci USA* 94: 14942–14947, 1997.
40. **Li Y, Asuri S, Rebhun JF, Castro AF, Paranavitana NC, Quilliam LA.** The RAP1 guanine nucleotide exchange factor Epac2 couples cyclic AMP and Ras signals at the plasma membrane. *J Biol Chem* 281: 2506–2514, 2006.
41. **Light PE, Manning Fox JE, Riedel MJ, Wheeler MB.** Glucagon-like peptide-1 inhibits pancreatic ATP-sensitive potassium channels via a protein kinase A- and ADP-dependent mechanism. *Mol Endocrinol* 16: 2135–2144, 2002.
42. **MacDonald PE, Salapatek AM, Wheeler MB.** Glucagon-like peptide-1 receptor activation antagonizes voltage-dependent repolarizing K(+) currents in beta-cells: a possible glucose-dependent insulinotropic mechanism. *Diabetes* 51, *Suppl* 3: S443–S447, 2002.
43. **Mathi SK, Chan Y, Li X, Wheeler MB.** Scanning of the glucagon-like peptide-1 receptor localizes G protein-activating determinants primarily to the N terminus of the third intracellular loop. *Mol Endocrinol* 11: 424–432, 1997.
44. **Meyer-Hermann ME.** The electrophysiology of the beta-cell based on single transmembrane protein characteristics. *Biophys J* 93: 2952–2968, 2007.
45. **Nauck MA, Heimesaat MM, Orskov C, Holst JJ, Ebert R, Creutzfeldt W.** Preserved incretin activity of glucagon-like peptide 1 [7–36 amide] but not of synthetic human gastric inhibitory polypeptide in patients with type-2 diabetes mellitus. *J Clin Invest* 91: 301–307, 1993.
46. **Nijholt IM, Dolga AM, Ostroveanu A, Luiten PG, Schmidt M, Eisel UL.** Neuronal AKAP150 coordinates PKA and Epac-mediated PKB/Akt phosphorylation. *Cell Signal* 20: 1715–1724, 2008.
47. **Oliveira RF, Terrin A, Di BG, Cannon RC, Koh W, Kim M, Zaccolo M, Blackwell KT.** The role of type 4 phosphodiesterases in generating microdomains of cAMP: large scale stochastic simulations. *PLoS One* 5: e11725, 2010.
48. **Pipeleers D.** The biosociology of pancreatic B cells. *Diabetologia* 30: 277–291, 1987.
49. **Ponsioen B, Gloerich M, Ritsma L, Rehmann H, Bos JL, Jalink K.** Direct spatial control of Epac1 by cyclic AMP. *Mol Cell Biol* 29: 2521–2531, 2009.
50. **Post SR, Hilal-Dandan R, Urasawa K, Brunton LL, Insel PA.** Quantification of signalling components and amplification in the beta-adrenergic-receptor-adenylate cyclase pathway in isolated adult rat ventricular myocytes. *Biochem J* 311: 75–80, 1995.
51. **Pyne NJ, Furman BL.** Cyclic nucleotide phosphodiesterases in pancreatic islets. *Diabetologia* 46: 1179–1189, 2003.
52. **Rehmann H, Arias-Palomo E, Hadders MA, Schwede F, Llorca O, Bos JL.** Structure of Epac2 in complex with a cyclic AMP analogue and RAP1B. *Nature* 455: 124–127, 2008.
53. **Roger B, Papin J, Vacher P, Raoux M, Mulot A, Dubois M, Kerr-Conte J, Voy BH, Pattou F, Charpentier G, Jonas JC, Moustaid-Moussa N, Lang J.** Adenylyl cyclase 8 is central to glucagon-like peptide 1 signalling and effects of chronically elevated glucose in rat and human pancreatic beta cells. *Diabetologia* 54: 390–402, 2011.
54. **Sams DJ, Montague W.** The role of adenosine 3′:5′-cyclic monophosphate in the regulation of insulin release. Properties of islet-cell adenosine 3′:5′-cyclic monophosphate phosphodiesterase. *Biochem J* 129: 945–952, 1972.
55. **Santos RM, Rosario LM, Nadal A, Garcia-Sancho J, Soria B, Valdeolmillos M.** Widespread synchronous $[Ca^{2+}]_i$ oscillations due to bursting electrical activity in single pancreatic islets. *Pflügers Arch* 418: 417–422, 1991.
56. **Saucerman JJ, Brunton LL, Michailova AP, McCulloch AD.** Modeling beta-adrenergic control of cardiac myocyte contractility in silico. *J Biol Chem* 278: 47997–48003, 2003.
57. **Suga S, Kanno T, Dobashi Y, Wakui M.** GLP-1 (7–36) amide activates L-type Ca^{2+} channels of pancreatic B-cells through c-AMP signaling. *Jpn J Physiol* 47, *Suppl* 1: S13–S14, 1997.
58. **Sunahara RK, Dessauer CW, Whisnant RE, Kleuss C, Gilman AG.** Interaction of Gsalpha with the cytosolic domains of mammalian adenylyl cyclase. *J Biol Chem* 272: 22265–22271, 1997.
59. **Syme CA, Zhang L, Bisello A.** Caveolin-1 regulates cellular trafficking and function of the glucagon-like Peptide 1 receptor. *Mol Endocrinol* 20: 3400–3411, 2006.
60. **Tengholm A, Gylfe E.** Oscillatory control of insulin secretion. *Mol Cell Endocrinol* 297: 58–72, 2009.
61. **Terrin A, Di BG, Pertegato V, Cheung YF, Baillie G, Lynch MJ, Elvassore N, Prinz A, Herberg FW, Houslay MD, Zaccolo M.** PGE(1) stimulation of HEK293 cells generates multiple contiguous domains with different [cAMP]: role of compartmentalized phosphodiesterases. *J Cell Biol* 175: 441–451, 2006.
62. **Thorens B.** Expression cloning of the pancreatic beta cell receptor for the gluco-incretin hormone glucagon-like peptide 1. *Proc Natl Acad Sci USA* 89: 8641–8645, 1992.
63. **Tsalkova T, Blumenthal DK, Mei FC, White MA, Cheng X.** Mechanism of Epac activation: structural and functional analyses of Epac2 hinge

mutants with constitutive and reduced activities. *J Biol Chem* 284: 23644–23651, 2009.

64. **Tsuboi T, da S, X, Holz GG, Jouaville LS, Thomas AP, Rutter GA.** Glucagon-like peptide-1 mobilizes intracellular Ca^{2+} and stimulates mitochondrial ATP synthesis in pancreatic MIN6 beta-cells. *Biochem J* 369: 287–299, 2003.
65. **Wheeler MB, Lu M, Dillon JS, Leng XH, Chen C, Boyd AE, III.** Functional expression of the rat glucagon-like peptide-I receptor, evidence for coupling to both adenylyl cyclase and phospholipase-C. *Endocrinology* 133: 57–62, 1993.
66. **Widmann C, Burki E, Dolci W, Thorens B.** Signal transduction by the cloned glucagon-like peptide-1 receptor: comparison with signaling by the endogenous receptors of beta cell lines. *Mol Pharmacol* 45: 1029–1035, 1994.
67. **Widmann C, Dolci W, Thorens B.** Desensitization and phosphorylation of the glucagon-like peptide-1 (GLP-1) receptor by GLP-1 and 4-phorbol 12-myristate 13-acetate. *Mol Endocrinol* 10: 62–75, 1996.
68. **Yan C, Zhao AZ, Bentley JK, Beavo JA.** The calmodulin-dependent phosphodiesterase gene PDE1C encodes several functionally different splice variants in a tissue-specific manner. *J Biol Chem* 271: 25699–25706, 1996.
69. **Yu X, Byrne JH, Baxter DA.** Modeling interactions between electrical activity and second-messenger cascades in Aplysia neuron R15. *J Neurophysiol* 91: 2297–2311, 2004.
70. **Zaccolo M, Pozzan T.** Discrete microdomains with high concentration of cAMP in stimulated rat neonatal cardiac myocytes. *Science* 295: 1711–1715, 2002.